Enhancing plain fatigue strength in aluminum alloys through shot peening: Experimental investigations and a strain energy density interpretation

M. Benedetti [a],[*], M. Pedranz [a], V. Fontanari [a], C. Menapace [a], M. Bandini [b]

[a] Department of Industrial Engineering, University of Trento, Italy
[b] PeenService, Bologna, Italy

ARTICLE INFO

ABSTRACT

This study addresses the complex interplay of shot peening-induced effects on the fatigue strength of high-strength aluminum alloys. The inherent poor fatigue properties of aluminum alloys, particularly exacerbated in components manufactured through additive processes, pose significant challenges. Shot peening, a recognized surface treatment, proves effective in enhancing fatigue resistance through mechanisms such as compressive residual stresses, work hardening, and microstructural changes. However, optimizing shot peening and developing accurate fatigue prediction models remain challenging due to the intricate and unclear contributions of the individual mechanisms. In this investigation, five distinct shot peening treatments were employed to emphasize specific effects. Experimental results, analyzed through a strain energy density approach, shed light on the crucial role of compressive residual stresses in maximizing fatigue strength. This comprehensive exploration contributes with valuable insights for designing shot peening treatments to optimize the fatigue performance of high-strength aluminum alloys.

1. Introduction

Among structural metals, aluminum alloys stand out for their impressive specific static strength but are marred by relatively poor fatigue properties [1,2]. This inherent limitation poses a significant challenge, especially when considering the prevalent use of aluminum alloys in critical engineering applications [3,4]. Such fatigue strength deficiency is further exacerbated when Al alloys are fabricated through additive manufacturing processes, primarily attributed to inadequate surface morphology [5] and internal defectiveness [6]. Within this context, shot peening, a widely acknowledged surface treatment, has demonstrated efficacy in overcoming the fatigue vulnerabilities of aluminum alloys [7,8]. This process involves bombarding a component's surface with small, high-velocity spherical shots, inducing a range of modifications such as the introduction of compressive residual stresses [9,10], work-hardening effects [11,12], and microstructural changes [12,13].

While the broad impact of shot peening is recognized, the nuanced details of the enhancing mechanisms remain elusive. On one hand, the detrimental effect of surface roughening on fatigue strength is evident, while on the other hand, the roles of grain refinement, work hardening,

and, significantly, residual stresses are subjects of ongoing debate. Some scholars correlate grain refinement and work hardening to the concept of microstructural barriers impeding the growth of microstructurally-small cracks [14]. In contrast, residual stresses are sometimes implicated in hindering crack nucleation due to the mean stress effect, while at other times, they are credited for retarding the growth of Physically-Small Cracks (PSC) by partially restoring crack closure, a phenomenon less developed in PSC compared to Long Cracks [15–17].

Amidst these uncertainties, comprehending and optimizing shot peening for fatigue improvement becomes a complex task, entangled in the intricate interplay of various factors. The challenge is exacerbated by the lack of clarity regarding how specific mechanisms within shot peening contribute to fatigue resistance. This knowledge gap impedes the development of accurate fatigue prediction models, hindering the optimization of shot peening processes tailored to specific materials and applications. As a result, various approaches have been explored to develop shot peening treatments targeting the enhancement of fatigue strength in Al alloys. Some strategies involve low-intensity treatments utilizing small beads to introduce minimal surface roughness and a thin layer of compressive residual stresses, strategically positioned with a peak in close proximity to the treated surface [18–20]. Conversely, other

---

* Corresponding author.
E-mail address: matteo.benedetti@unitn.it (M. Benedetti).

methodologies employ intense peening treatments utilizing larger shots, some even composed of steels [21,22], with the objective of inducing deeper compressive residual stress profiles and heightened work hardening, aimed at stabilizing the residual stresses during the component service life. Additionally, high-intensity, high-coverage processes have been investigated, focusing on inducing grain recrystallization coupled with the refinement of the grain structure down to the nanoscale [10,23,24].

The ambiguity surrounding the fatigue-related effects of shot peening is reflective of the diverse methodologies employed to calculate the fatigue strength of shot-peened components. Generally, appropriate multiaxial fatigue criteria are employed, integrating residual stresses as mean stresses superimposed on the stress field generated by external loading [25–28]. Sometimes, residual stresses are incorporated into fatigue calculations not only by assuming that the fatigue life is predominantly spent initiating small cracks but also by adopting total fatigue life approaches that account for the retardation effect of residual stress on crack propagation [29,30]. Recently, an alternative perspective on residual stresses has been proposed, replacing the concept of residuals as mean stresses with that of an independent stress field that produces negative specific work when exposed to mechanical strains. This work is then encapsulated into a strain energy density-based fatigue calculation framework [31]. To address the adverse impact of surface roughness, a common practice is the utilization of a semi-analytical stress concentration factor [32], often disregarding the material's notch sensitivity. In more recent developments, finite element simulations of the roughness profiles of shot-peened components have been conducted to evaluate the stress concentration factor induced by roughness [12]. This is sometimes coupled with a critical distance approach to incorporate material notch sensitivity [25]. Moreover, the microstructural effects induced by shot peening on the fatigue properties of the outer layers [12] are sometimes considered. This involves the use of empirical correction coefficients primarily based on the full-width-at-half-maximum (FWHM) of diffraction peaks [33,34]. Lastly, it is noteworthy that certain studies in the past have uncovered a dualism in the crack initiation sites of shot-peened Al alloys, particularly in plain (unnotched) samples subjected to very-high-cycle fatigue testing. Specifically, crack initiation has been observed not only near the treated surface but also beneath the surface layers affected by shot peening [20,35,36]. The incorporation of these various elements into fatigue prediction models underscores the complexity of understanding and optimizing shot peening processes for enhanced fatigue performance, highlighting the critical need for a comprehensive and integrated approach to accurately model and predict fatigue strength in shot-peened components.

The central objective of this study is to further investigate the importance of the aforementioned shot-peening related effects, aiming to identify optimal treatments and effective fatigue calculation models for high-strength Al alloys. To achieve this goal, five different shot peening treatments have been considered, each one emphasizing a specific effect. Two low-intensity treatments employing small shots have been devised to introduce similar in-depth residual stress profiles while inducing different surface roughness and work hardening. A conventional treatment with higher intensity and larger shots has been applied to introduce a deeper residual stress profile. Finally, a high-coverage treatment, either standalone or in combination with the previous one, has been applied to induce grain refinement into the surface layer.

The article is structured as follows: Section 2 provides a detailed description of the investigated material variants and outlines the experimental techniques employed to characterize the material modifications induced by shot peening. In Section 3, we present the experimental results, which are subsequently interpreted in the context of a strain energy density approach proposed in a prior study [31], briefly summarized in Section 4. The latter section also encompasses a description of the numerical analyses conducted to assess the influence of residual stresses and surface roughness. Section 5 delves into the discussion of the results obtained through the proposed fatigue

calculation approach, offering insights into the design of shot peening treatments capable of maximizing fatigue strength improvement. Concluding remarks are presented in Section 6.

2. Experimental materials and methods

The experimentation was carried out on specimens extracted from extruded bars of aeronautical Al grade 7075-T6 with a diameter of 60 mm. The raw material supplier declared that both heat treatment (solubilization at 470 °C for 1 h followed by water quenching and aging at 120 °C for 24 h) and chemical composition were compliant with the material standard.

Monotonic tensile tests (initial strain rate of 10^{-4} s^{-1}) were performed according to the standard ASTM E8 on dog-bone axisymmetric specimens (gage diameter 6 mm) aligned with the longitudinal (L) orientation of the bars. Three tests were replicated room temperature (25C, 60 % R.H.) using a servo-hydraulic universal testing machine INSTRON 8516, equipped with hydraulic grips, a load cell of 100 kN (non-linearity ±0.1 % of rated output R.O.), and an axial extensometer (10 mm gauge length, nonlinearity ±0.15 % of R.O.). The yield strength was determined based on the 0.2 % offset method. The results of the tensile tests, as listed in Table 1, align with the minimum requirements outlined in DIN EN 755–2. Furthermore, they closely resemble the values reported in [37] for the same alloy obtained from extruded bars of identical dimensions. The reader is referred to [37] for a detailed microstructural analysis of grain size and intermetallic precipitates dispersion.

To assess the high-cycle fatigue (HCF) behavior, 8-point bending fatigue tests were carried out in the longitudinal (L) orientation using hourglass axisymmetric specimens, as illustrated in Fig. 1a, with a minimum gage diameter of 5 mm. These tests adhered to the ASTM E466 standard. Notably, the specimens featured a fillet radius sufficiently large to minimize any notch fatigue effects (theoretical stress concentration factor $K_t = 1.02$). The intentional selection of axisymmetric geometry aimed to eliminate stress perturbation effects, which often localize fatigue crack initiation near the edges in prismatic specimens [18]. To facilitate testing under 8-point bending fatigue loading, the terminal part of the specimens was flattened through milling.

A subset of the specimens underwent controlled shot peening, and the parameters for the five peening treatments are outlined in Table 2. Each treatment, administered with a 90° angle of impingement using an air-blast machine, aimed to explore potential fatigue-related effects arising from (i) peening-induced microstructural changes and (ii) the introduction of grain refinement down to nanoscale into the outermost surface layers. For the first objective, two shot peening treatments, denoted as UFS50 100 % and Z100 100 %, were implemented. Despite having nominally identical intensity and coverage, these treatments utilized shots of significantly different sizes. In particular, ultra-fine steel shots are employed in UFS50 100 %. This intentional contrast aimed to yield a very similar in-depth residual stress profile while inducing distinct surface roughness and plastic deformation. In the third treatment, denoted as Z100 1000 %, process parameters mirrored those of the second treatment, except for an extended treatment time to achieve 1000 % coverage and induce grain refinement in the surface layers, as previously observed in [24]. A second grain refinement approach involved a double peening treatment. Initially, a conventional treatment

Table 1
Monotonic tensile properties based on three replicated tests with respect to the rolling direction.

E (GPa)	σ_Y (MPa)	σ_U (MPa)	*T.E.* (%)	*U.E.* (%)
69.0 ± 0.1	487 ± 7	570 ± 5	10.5 ± 0.6	7.6 ± 0.2

Note: Standard error corresponds to 1σ uncertainty band.
Abbreviations: *E*, Young's modulus; σ_U, ultimate tensile strength; σ_Y, 0.2% yield stress; *T.E.*, total elongation; *U.E.*, uniform elongation.
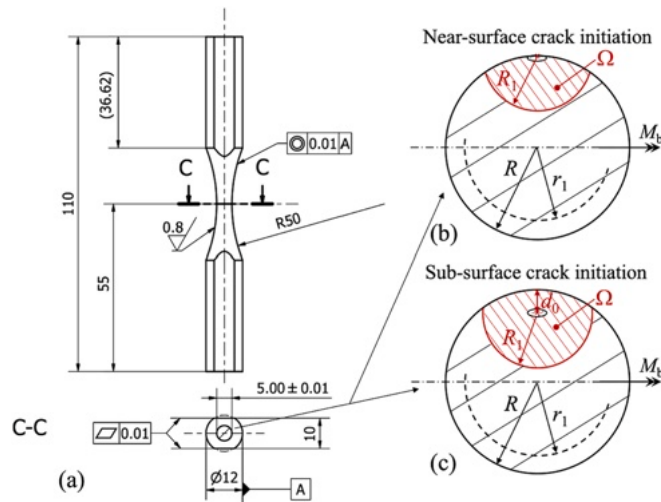
Fig. 1. Geometry of the axisymmetric hourglass samples used for the 8-point bending fatigue tests. Dimensions are given in mm. M_b indicates the axis of application of the bending moment. The SED-averaging control domain Ω is centered either on the outer tensioned side of the specimen (b) or at distance d_0 from this location (c). d_0 indicates the effective depth of the peening treatment. R denotes the specimen gage diameter (=5 mm) and r_1 denotes the radial coordinate of the removed layer during XRD residual stress measurements.

Table 2
Parameters of the five shot peening treatments considered in this study.

Condition	Shot material	Bead size (mm)	Almen intensity	Coverage (%)
UFS50 100 %	Steel	40–70	11 N	100
Z100 100 %	Ceramic	100–150	11 N	100
Z100 1000 %	Ceramic	100–150	9 N	1000
Z425 100 %	Ceramic	425–600	5A	100
Z425 + Z100	Ceramic	425–600 + 100–150	5A + 9 N	100 + 1000

was conducted using large ceramic beads (Z425 100 %), followed by treatment Z100 1000 %. Lastly, the sole effect of Z425 100 % was examined as a dedicated experimental variant.

Fully-reversed (R = −1) load-controlled fatigue tests were conducted in ambient air at room temperature. The tests were executed using a resonant testing machine, Rumul Miktrotron 20 kN, operating at a nominal frequency of 90 Hz and equipped with a preloaded 8-point bending fixture. The fatigue tests continued until specimens either experienced failure or reached a pre-established fatigue life, set at 3×10^7 cycles. Run-out specimens were subjected to reuse, enduring an applied load at least 1.5 times higher than the original, thereby extending the dataset and enhancing the experimental data points for non-linear fitting of the S-N fatigue curves. A total of 15 tests were performed, with 2–3 tests replicated at each load step. The Wöhler's curves were fitted using Eq. (1).

$$\sigma_a = c_1 + \frac{C_2}{N_f^{c_3}} \qquad (1)$$

where c_1, c_2, and c_3 are fitting parameters, N_f is the number of cycles upon failure or runout and σ_a is the stress amplitude. The scatter bands at 10 % and 90 % failure probability are also reported and have been calculated considering a uniform regression variance throughout the whole tested range. These bands can be consequently calculated as follow in Eq. (2)

$$S^2 = \frac{\sum_{i=1}^{n} \left(\sigma_{a,i} - \widehat{\sigma}_{a,i} \right)^2}{n - p} \qquad (2)$$

where $\sigma_{a,i}$ is the i.th fatigue amplitude, $\widehat{\sigma}_{a,i}$ its estimator. The parameters, n and p, are the numbers of collected data and the number of regression parameters involved in Eq. (1) thus set to 3.

Fatigue fracture surfaces have been investigated using a JEOL JSM-IT300LV scanning electron microscope (SEM) to identify the location of the fatigue crack initiation site. For the metallographic analyses, coupons cut in longitudinal direction from the fatigue samples were cold mounted in resin, polished, and etched with a solution of nitric acid (15.5 ml), hydrofluoric acid (0.5 ml) and chromium trioxide (3 g) in 84 ml of distilled water. The specimens were examined using both SEM and a light optical Zeiss Axiophot microscope. The polishing step was carried out with cloths of 1 μm and 0.04 μm with OPS solution to assure a perfect surface preparation, removing all residual scratches due to grinding.

The alterations in surface layers resulting from the shot peening treatments were systematically investigated through measurements of microhardness, surface roughness and residual stress profiles. Microhardness in-depth profiles were measured on the metallographic sections using a Vickers indenter under a load of 0.025 kgf. Three measurements were performed at each depth and averaged to account for material's heterogeneity and measurement errors.

Surface morphology examinations were conducted using an Olympus DSX100 High-Resolution Opto-digital microscope, equipped with a 20x objective lens. The DSX10-BSW software facilitated surface roughness analysis. Each specimen underwent scanning along the longitudinal direction, with measurements taken on both cylinder generatrices (the curves describing the cylinder surface when rotated about its axis) experiencing the highest bending stress. To adhere rigorously to ISO standards (ISO 4288:1996), an evaluation length of 12.5 or 4 mm and a cut-off wavelength (λ_c) of 2.5 or 0.8 mm were selected for surface profiles with Rz larger or lower to 10 μm, respectively. The profile mean line was derived by fitting the measured surface profile with an equation representing the circular arc of the hourglass part of the specimen. For the assessment of surface roughness parameters, the mean line was subtracted from the measurements, and the resultant data were filtered using a Gaussian filter with a kernel size of λ_c to eliminate the contribution of waviness.

Residual stress analysis was carried out using the X-ray Diffraction (XRD) technique, employing an AST X-Stress 3000 X-ray diffractometer. Measurements were conducted with Cr $K\alpha$ radiation in the longitudinal direction within the gage region. The analysis zone was restricted by a collimator with an area of 1 mm². For stress evaluation, the classical $\sin^2\psi$ method was employed, utilizing 9 diffraction angles (2θ) scanned between −45° and +45° for each stress value. The ⟨311⟩ diffracting planes were specifically chosen for two reasons: (i) to obtain high angle measurements (2θ angle 139.0°) with increased strain sensitivity, and (ii) because they do not accumulate significant intergranular stresses, exhibiting behavior like that of the bulk material. The system calibration was validated by obtaining a diffraction pattern from a standard polycrystalline Al powder before the commencement of the experiment. In-depth measurements were conducted on peened specimens that were not subjected to fatigue testing to assess the initial residual stress field. For this purpose, material was incrementally removed from the specimen surface using an electrochemical method to avoid introducing additional residual stress. Specifically, a Struers - Movipol electro polisher was utilized with a diluted perchloric acid solution and a voltage of 40 V. The procedure involved placing the specimen in the material removal station, activating the Movipol probe on the surface, and initiating the acid solution and electrical current. Once the desired time elapsed, the specimen was measured with a linear gauge to verify the amount of material removed. This process was repeated until the desired material removal amount was achieved.

In-depth residual stress profiles were corrected to address the impact

of the removed layer on the residual stress field using the expression reported in [38] specifically designed for rotationally symmetric residual stresses in axisymmetric bodies:

$$\sigma_{zz}^{RS}(r_1) = \sigma_{zz,m}^{RS}(r_1) - 2\int_{r_1}^{R-r_1}\frac{\sigma_{zz,m}^{RS}(r)}{r}dr \qquad (3)$$

where R is the specimen outer radius, r_1 is the radial coordinate of the surface exposed after layer removal (see Fig. 1b and c), where the axial stress $\sigma_{zz,m}^{RS}(r_1)$ is measured.

In the course of residual stress measurements, the Full Width at Half Maximum (FWHM) parameter was also determined. FWHM is calculated as the width of the diffraction peak at half of its maximum height and is directly linked to the value of residual microstrain (Type II) present in the material. The FWHM parameter exhibits sensitivity to multiple microstructure parameters, including crystallite size (coherently diffracting areas), non-oriented microstress, and dislocation density. In this specific case, it is deemed in some investigations [24,33] as an indicator of work hardening at the microscopic scale within the material.

3. Experimental results

3.1. Microstructure and surface morphology

Fig. 2 presents representative etched SEM micrographs illustrating the microstructure of the surface layers in the fatigue samples. It is worth noting that the treatments employing the largest shots with standard coverage (Z100 100 %, Fig. 2c, and Z425 100 %, Fig. 2e) did not appreciably modify the microstructure of the surface layers when compared to the as-received condition (Fig. 2a). These treatments maintained a very similar grain size and precipitate distribution. Conversely, the ultra-fine shot particle treatment (UFS50 100 %, Fig. 2b) and, to a significantly greater extent, the two treatments employing very large coverage values (Z100 1000 %, Fig. 2d, and Z425 + Z100, Fig. 2f), considerably altered the microstructure of the outermost layers, inducing grain refinement and denser dispersion of finer intermetallic precipitates. Notably, these three material variants are characterized by a brighter (10 to 25 μm thick) surface layer, representative of a more reactive microstructure produced by the work hardening introduced by such shot peening treatments.

Unetched optical micrographs are presented in Fig. 3 to reveal

possible defects introduced by the peening treatment into the surface layers. Notably, the three variants employing Z100 shots (Z100 100 %, Fig. 3c, Z100 1000 %, Fig. 3d, Z425 + Z100, Fig. 3f) result in the peeling-off of material layers due to their intense plastic deformation, leading to the formation of crack-like defects on the surface. This phenomenon is of much lower extent in UFS50 100 % (Fig. 3b) and practically absent in the Z425 100 % variant (Fig. 3e).

The results of the surface roughness measurements are summarized in Table 3. It is noteworthy that the *Ra* roughness of the as-received condition complies with the specified requirement in the specimen drawing presented in Fig. 1a. All the peening treatments result in an increase in surface roughness, exhibiting a discernible general trend of increment with increasing shot size. Interestingly, an increment in coverage did not produce an appreciable increase in roughness.

3.2. In-depth residual stress and microhardness profiles

In Fig. 4a and b, the in-depth measurements of longitudinal residual stress, FWHM, and microhardness are illustrated. Looking at Fig. 4a, it is evident that the depth of surface layers influenced by residual stresses and strains (expressed in terms of FWHM) primarily depends on the shot size, with the highest depth observed when employing the largest shots, Z425. In practical terms, considering the peening effects extinguished when the residual stresses drop below −50 MPa and FWHM below 1.5°, an effective peening depth (d_0) of approximately 70 μm characterizes the treatments UFS50 100 %, Z100 100 %, and Z100 1000 %. d_0 increases to about 190 μm for Z425 100 % and to 250 μm for the double treatment Z425 + Z100. The deepest compressive residual stress peaks are exhibited by Z100 100 % and Z425 100 %. Interestingly, the application of a high-coverage treatment in Z100 1000 % and Z425 + Z100 leads to less intense compressive residual stresses and strains on the surface.

The scenario depicted by Fig. 4b in terms of the in-depth microhardness profile is distinctly different. All peening treatments yielded microhardness profiles that are virtually indistinguishable from the as-received condition. In fact, all the data fall within a scatter band centered around the mean value of the as-received condition, with a width equal to ±3 times the standard deviation of the same data. Only the UFS50 100 % treatment displays a discernibly higher microhardness value in the immediate surface layer. This is likely attributed to the combination of a higher impact velocity and finer shot size, enabling deeper indentation into the surface layers. The relatively modest
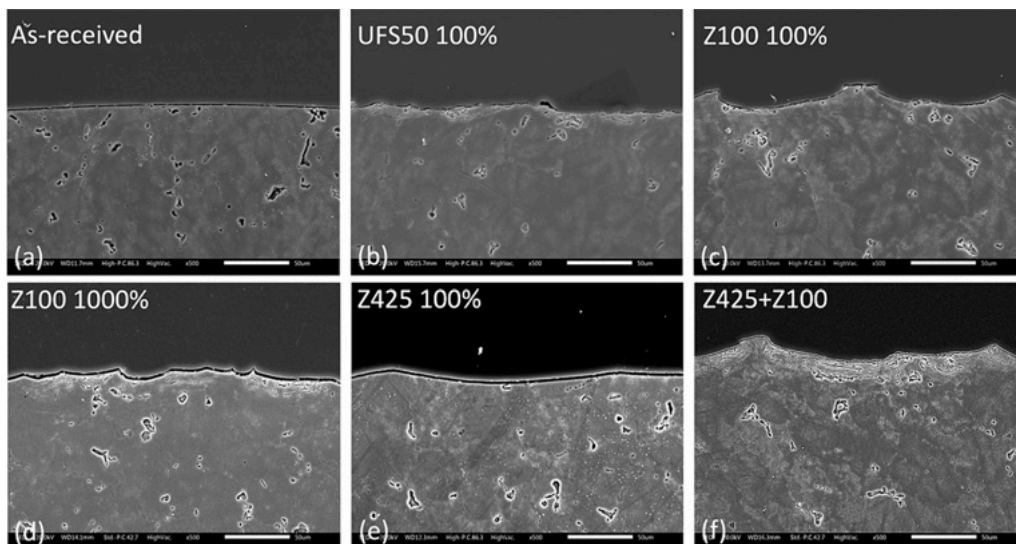

Fig. 2. Etched SEM micrographs of the microstructure of the surface layers of the fatigue samples revealing the material microstructure. (a) As-received condition, (b) UFS50 100 %, (c) Z100 100 %, (d) Z100 1000 %, (e) Z425 100 %, (f) Z425 100 % + Z100 1000 % shot peened conditions.

Fig. 3. Unetched optical micrographs of the microstructure of the surface layers of the fatigue samples revealing the surface morphology. (a) As-received condition, (b) UFS50 100 %, (c) Z100 100 %, (d) Z100 1000 %, (e) Z425 100 %, (f) Z425 100 % + Z100 1000 % shot peened conditions.

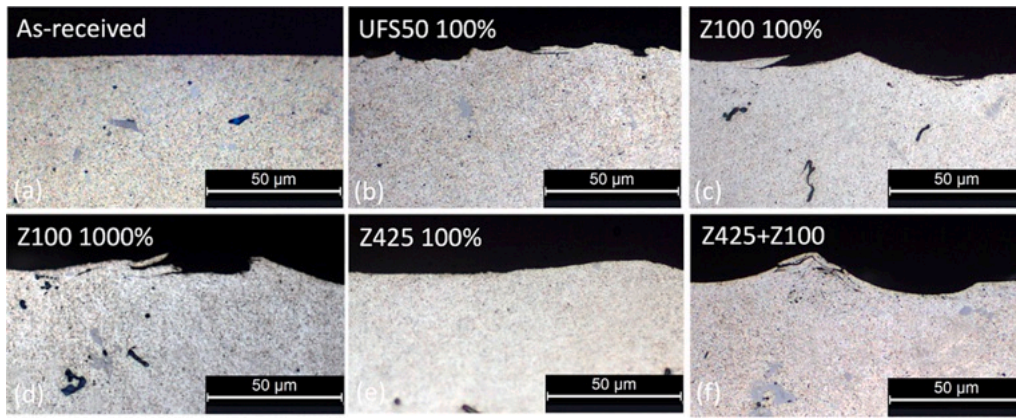**Table 3**
Surface roughness properties. *Ra*: average roughness; *Rq*: root mean square roughness; *Rz*: average maximum height of the profile; *Rv*: maximum profile valley depth, *Rp*: maximum profile peak height.

Condition	Ra (μm)	Rq (μm)	Rz (μm)	Rv (μm)	Rp (μm)
As-received	0.87	1.04	5.82	2.92	1.90
UFS50 100 %	1.16	1.47	8.45	3.63	4.82
Z100 100 %	1.34	1.72	10.05	4.94	5.11
Z100 1000 %	1.36	1.71	10.87	5.88	4.99
Z425 100 %	2.15	2.66	14.72	6.69	8.03
Z425 + Z100	2.04	2.59	16.05	8.21	7.84

increase in microhardness, despite the higher work hardening observed through XRD measurements, may be attributed to the low strain-hardening behavior of the investigated material. Additionally, the divergence in scales between microhardness and FWHM measurements may capture the material's work hardening differently.

3.3. Fatigue results and fractographic analyses

The results of the fatigue tests carried out on all the specimen variants are compared in Fig. 5 and detailed in Appendix A. Fitting curves corresponding to 50 % (thick line), 10 % and 90 % (dotted thin lines enclosing a colored scatter band) failure probability, expressed by Eq. (1), are also plotted in Fig. 5. The best-fit parameters, the standard deviation *S*, the fatigue strength at 3×10^7 cycles and the corresponding

gain of the shot peened variant with respect to the unpeened counterpart are listed in Table 4.

All the considered peening treatments proved effective in prolonging the fatigue life of the material. This improvement depends on the applied load, with more remarkable enhancements observed for load levels corresponding to longer fatigue lives. It can also be observed that, in line with previous investigations on similar treatments [18], the highest fatigue performance improvements were achieved by the gentlest treatments UFS50 100 % and Z100 100 %. Surprisingly, the application of the most intense treatment Z425 100 %, even in combination with Z100 1000 %, resulted in the lowest increment in fatigue strength. The increase in coverage adopted in Z100 1000 % led to an intermediate enhancement of fatigue strength.

The fracture surfaces of the specimens marked with a circle in Fig. 5 were analyzed using a scanning electron microscope (SEM). Fig. 6 depicts the region surrounding the fatigue crack initiation site marked by an arrow. d_i and d_0 denote the distance from the surface of the detected fatigue crack initiation site and the effective depth of the shot peening treatment (see Fig. 4a), respectively. It can be noted that, owing to the bending stress distribution, surface crack initiation occurs in the as-received condition (Fig. 6a). Near-surface crack initiation is observed in the variants employing small shots (UFS50 100 %, Fig. 6b, Z100 100 %, Fig. 6c, Z100 1000 %, Fig. 6d), with the initiation site located at a distance d_i of 0.1 mm below the surface. In this case, d_i is well correlated to the effective treatment depth d_0 identified based on the residual stress and strain profiles depicted in Fig. 4a. On the contrary, the two variants
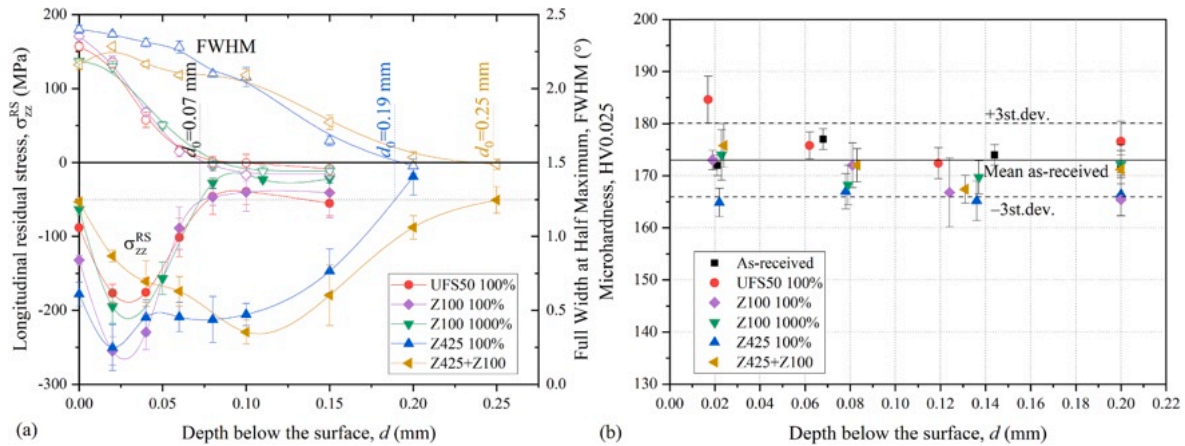

Fig. 4. (a) In-depth residual stress and Full Width at Half Maximum (FWHM) profiles determined using a XRD technique. (b) Microhardness in-depth profiles. The solid line indicates the average microhardness measured in the as-received condition throughout the explored surface layer. The dashed lines denote the band with width equal to ±3 times the standard deviation of the same data.
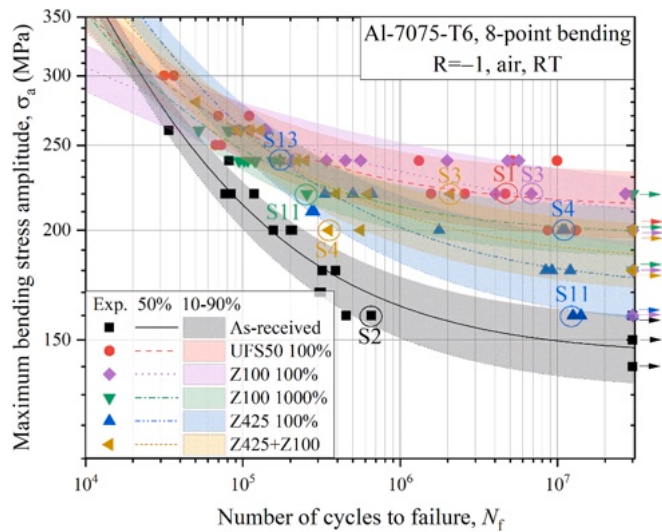
Fig. 5. Fully-reversed 8-point bending fatigue SN curves. Solid lines represent 50% failure probability, while dashed lines refer to 10% and 90% failure probability. Arrows indicates runout tests. Circled fatigue data indicates specimens whose fracture surface were analyzed with a scanning electron microscope (see Fig. 6).

resulting in a deeper penetration depth d_0 (Z425 100 %, Fig. 6e-g, Z425 + Z100, Fig. 6h-i) are characterized by a larger dispersion in the depth d_i of the crack initiation site. Indeed, this is either located near the treated surface or approximately in the correspondence of the treatment penetration depth d_0. Anyway, in none of the peened variants, fatigue crack initiation was observed in the correspondence of the treated surface. This underscores the effectiveness of shot peening fatigue-enhancing mechanisms in neutralizing the potential impact of the surface pile-up defects documented by metallographic analysis in certain shot-peened variants.

The dualism in the location where fatigue cracks originate will be integrated into the interpretative fatigue calculation model, which will be developed and discussed in the next section.

4. An interpretative model

4.1. SED fatigue criterion

In this section, we will provide a brief summary of the average strain-energy–density (ASED) criterion devised in [31] for fatigue calculations in the presence of residual stresses. This criterion specifically accounts for the energetic contributions of externally applied mechanical strains and residual stresses separately. The contribution from externally applied mechanical strains includes an equivalent fatigue damage parameter that incorporates the range $\Delta \overline{W}$ and the maximum value $\overline{W}_{\max}$ of ASED (Fig. 7a). The contribution from residual stresses is encapsulated in the form of the specific work done by residual stresses in the presence of fluctuating mechanical strains $\overline{W}^{RS}$. Its definition in the case of uniformly distributed uniaxial residual stress and mechanical strain is

illustrated in Fig. 7b and expressed as follows:

$$W^{RS} = \sigma^{RS} \Delta \varepsilon^+ \tag{4a}$$

$$\Delta \varepsilon^+ = \begin{cases} \varepsilon_{\max} - \varepsilon_{\min} & \varepsilon_{\min} > 0 \\ \varepsilon_{\max} & \varepsilon_{\min} \leq 0 \end{cases} \tag{4b}$$

and can be generalized for multiaxial stress–strain fields. Importantly, it is worth noting that only the positive range of mechanical strains is considered here, under the reasonable assumption that the beneficial effect exerted by compressive residual stresses in the presence of compressive mechanical strains is negligible.

The resulting fatigue criterion can be expressed as follows:

$$\Delta \overline{W}^\alpha \overline{W}_{\max}^{1-\alpha} + \overline{W}^{RS} = \Delta \overline{W}_1 \tag{5}$$

Notably, the presence of compressive residual stresses makes the specific work $\overline{W}^{RS}$ negative and results in an increment of the fatigue strength predicted by Eq. (5). The overbar sign indicates that the two SED components $\Delta \overline{W}$ and $\overline{W}_{\max}$ as well as $\overline{W}^{RS}$ are averaged over a control domain Ω of material characteristic size. In the present work, similar to what was done in our previous study [31], Ω will be considered a two-dimensional averaging domain lying on the minimum gage cross-section of the specimen (C–C in Fig. 1a). Specifically, it will be assumed to be a circular domain of radius R_1 centered either at the point on the outer surface experiencing the highest bending stress (Fig. 1b) or at a point shifted, with respect to this location, by the treatment effective depth d_0 beneath the surface (Fig. 1c). The former represents a near-surface, and the latter a sub-superficial crack initiation scenario, aligning with the fractographic investigations reported in Section 3.3.

The mean stress sensitivity factor $1 - \alpha$, the control radius R_1 and the fatigue strength characteristic $\Delta \overline{W}_1$ are material-dependent constants, which are assumed to depend only on the number of cycles to failure N_f. Their calibration was previously conducted in [39] on a very similar Al-7075-T6 alloy based on axial fatigue experiments performed on plain and notched specimens tested at different load ratios [40]. The results thereof are plotted in Fig. 8a and b, respectively, and will be used to predict the fatigue strength of the material variants tested in the present work. Note that these parameters were evaluated using unpeened specimens and therefore they do not incorporate the effect of grain refinement and work hardening induced by shot peening, which will be assumed to exert a negligible effect on the fatigue response.

The ASED terms of Eq. (5) were calculated through finite element (FE) simulations of the residual and mechanical stress fields present in the samples, as discussed in Section 4.2.

4.2. FEM simulations

In this section, we will present the finite element (FE) models used to assess mechanical stresses and their interaction with the residual stress field (Fig. 9a-c), as well as the effect of surface roughness on the stress field of the outer layers (Fig. 9d-f).

In the first case, linear brick elements (SOLID185) available in the commercial software Ansys© were used to discretize one quarter of the hourglass part of the specimen geometry by imposing suitable symmetry

Table 4
Best-fit coefficients of Eq. (1) used to interpolate the SN curves. S indicates the standard deviation. Gain indicates the increment in high-cycle fatigue strength with respect to the as-received condition.

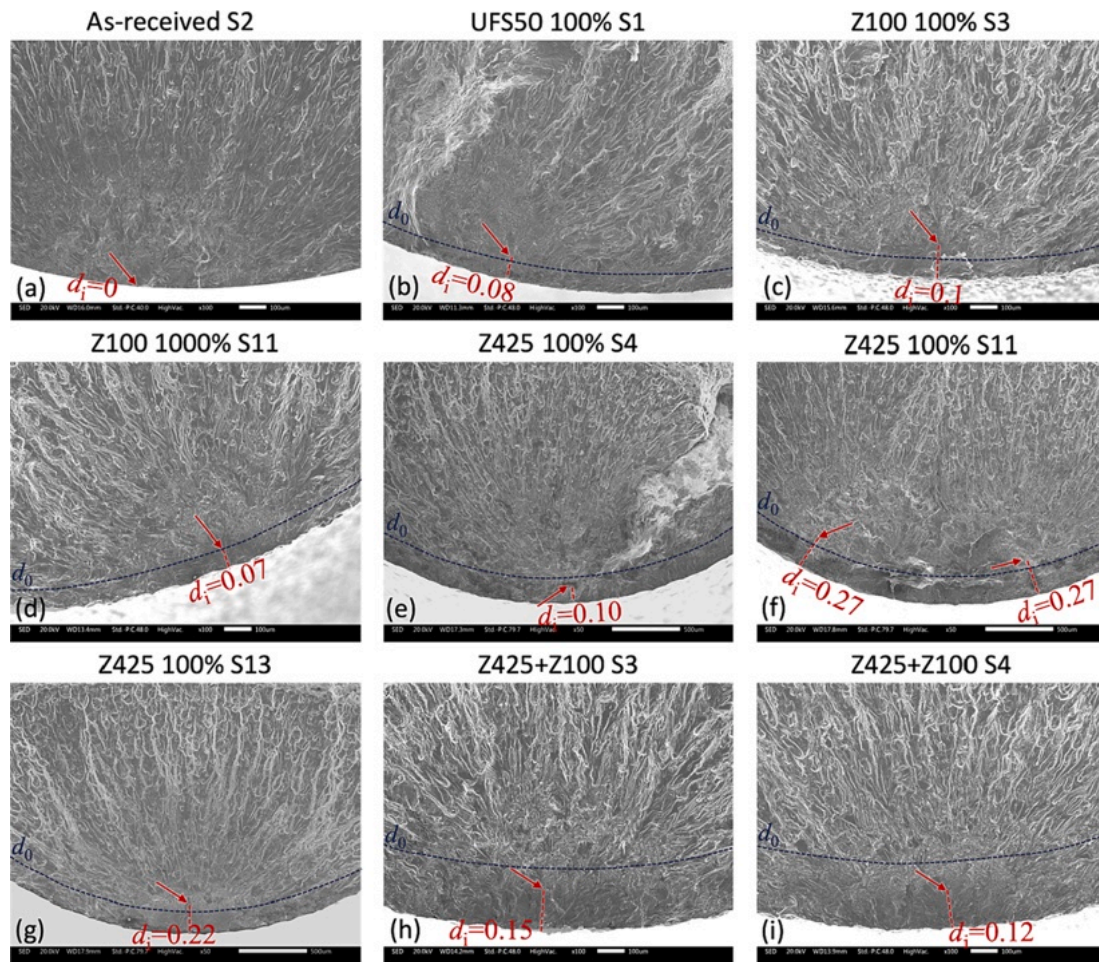| Condition	c_1 (MPa)	c_2 (MPa)	c_3	Standard deviation, S (MPa)	$\sigma_{a,3 \times 10^7}$ (MPa)	Gain (%)
As-received	144	35,938	0.542	10	147	–
UFS50 100 %	211	12,341	0.482	15	215	46
Z100 100 %	190	846	0.215	15	211	43
Z100 1000 %	197	15,450	0.498	9.9	200	36
Z425 100 %	170	18,378	0.461	14	177	20
Z425 + Z100	182	14,778	0.459	12	188	28

Fig. 6. SEM micrographs of the fracture surfaces around the fatigue crack initiation site of selected fatigued specimens. Stress amplitude and number of cycles to failure can be deduced from Fig. 5. (a) As-received, (b) UFS50 100 %, (c) Z100 100 %, (d) Z100 1000 %, (e-g) Z425 100 %, (h-i) Z425 + Z100. The dashed line indicates the effective depth d_0 of the shot peening treatment (see Fig. 4a).
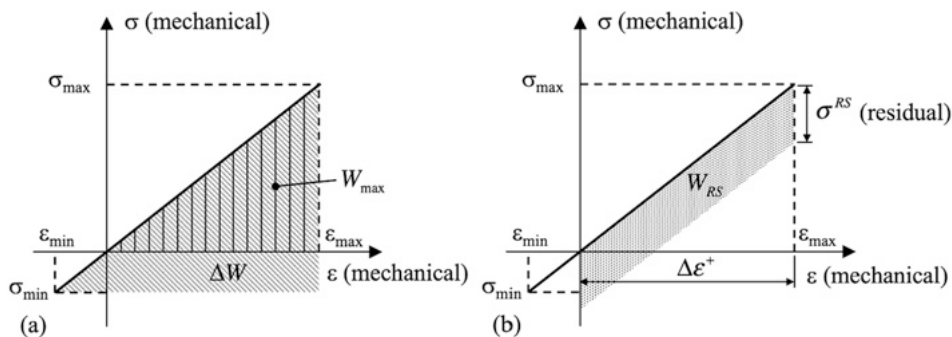

Fig. 7. Definition of the strain energy density components considered in the fatigue criterion. (a) Components of strain energy density associated with external mechanical loading, including the SED associated with the stress range ΔW (obliquely dashed area) and the maximum SED, W_{max} (vertically dashed area). (b) Specific work, W^{RS}, representing the energy expended under fluctuating positive mechanical strains in the presence of residual stresses. Readapted from [31].

constraints (Fig. 9a). A mapped mesh scheme was adopted to minimize element distortion. The mesh was particularly refined on the outer layer, with an element characteristic size of 0.012 mm, to capture the intense residual stress gradients introduced by the peening treatments. Residual stresses were introduced into the model according to the Eigenstrain method elucidated in [41,42]. In brief, this method involves applying misfit strains produced by a fictitious temperature distribution, assumed to be rotationally symmetric and a function of only the depth below the surface. The intensity of the temperature field is fitted from the

experimental in-depth residual stress measurements shown in Fig. 4a. For this purpose, an influence matrix correlating the axial residual stress produced in the j-th layer by a unitary temperature applied to the i-th layer was numerically computed. Its pseudoinverse is multiplied by the residual stress measures to determine the requested temperature field. This is then applied as body thermal loads to the FE model, as shown in Fig. 9b.

Stabilized residual stresses, found in [25,31] to be better correlated with the actual fatigue strength of the peened samples, were computed
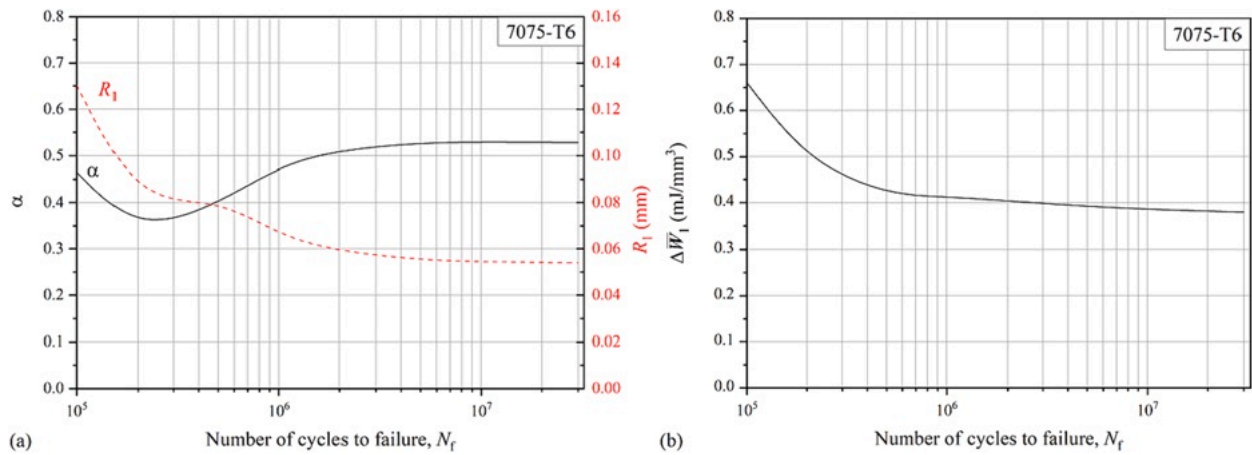
Fig. 8. Dependency of the parameters of the ASED fatigue criterion on the number of cycles to failure. Their calibration was performed in [39] on a very similar Al-7075 alloy. (a) mean stress sensitivity factor $1 - \alpha$ and control radius R_1, (b) fatigue strength characteristic $\Delta \overline{W}_1$.

by simulating the elastic–plastic stress redistribution produced by the application of the mechanical stresses. This approach, as demonstrated in [42], has been proven to assess stabilized residual stresses in very good agreement with experimental measures taken on fatigued specimens. For this purpose, the bending fatigue load was applied to the terminal part of the model in the form of a pressure distribution that varies linearly with respect to the distance from the neutral axis (see Fig. 9a). The material behavior was represented through a rate-independent, incremental theory of plasticity based on the Von Mises yield surface model with an associated plastic flow rule. The hardening rule is given by the superposition of three Chaboche kinematic hardening submodels. The Chaboche parameters, listed in Table 5, were deduced using an efficient identification procedure devised in [43] and applied to stabilized stress–strain hysteresis loops determined in [37] from strain-controlled cyclic tests conducted on a very similar 7075-T6 alloy. Fully-reversed time-varying bending loading was simulated until residual stress stabilization, which occurred after about 10–20 load cycles. The comparison of numerically evaluated initial and stabilized residual stresses under varying bending stress amplitudes is presented in Fig. B1 of Appendix B.

The average SED components and specific work done by residual stresses were directly computed from the subset of elements (depicted in Fig. 9c) belonging to the control domain Ω and lying on the specimen symmetry plane. According to the approaches sketched in Fig. 1b and c, the center of Ω was either located on the surface or below it at a distance d_0. Specifically, the SED components were calculated and stored using *ad-hoc* Ansys Parametric Design Language (APDL) scripts. The range (maximum value) of the SED associated with mechanical loading was estimated for each element lying in the control volume. These element SED components were finally averaged over the control volume to evaluate $\Delta \overline{W}$ and $\overline{W}_{max}$. Another *ad-hoc* APDL routine was used to extract the positive range of elastic strains and the corresponding residual stress components, whereby $\overline{W}^{RS}$ was averaged over the domain Ω. The variation of the size R_1 of Ω upon the fatigue life (see Fig. 8a) was considered in the assessment of the averaged strain and work density and incorporated into the fatigue predictions.

To keep the computational cost affordable, the solid model shown in Fig. 9a-c assumed a perfectly smooth outer surface. The effect of surface roughening induced by shot peening on the fatigue strength was evaluated separately. For this purpose, the axisymmetric model illustrated in Fig. 9d-f was used. The outer surface of the model was obtained by importing the surface profile acquired using the optical microscope described in Section 2. The surface profile was only corrected by subtracting the hourglass curvature of the specimen without any other filtering process. This approach involved establishing a straight surface

midline, specifically designed to isolate and assess the exclusive contribution of surface roughness to the stress field. The model was discretized with a free mesh of harmonic quadratic elements (PLANE83) capable of simulating a non-axisymmetric bending load, which was introduced through a linear distribution of pressures applied to the terminal part of the model. The mesh was particularly refined in the vicinity of the rough surface, with an element characteristic size equal to the spatial pitch (about 1.5 μm) with which the roughness height was sampled. The notch effects exerted by surface irregularities were captured by adopting, once again, an averaged SED approach. For this purpose, the circular averaging domain Ω was centered at the surface location of the model displaying the highest equivalent von Mises stress (Fig. 9e). Contrary to prior axisymmetric analyses where Ω was considered as a toroidal volume [44], in the current case Ω represents a planar domain situated on the radial plane that undergoes the highest bending stresses. The SED in the elements comprised within Ω (Fig. 9f) was used to compute the roughness-averaged SED $\overline{W}_{rough}$. This procedure was iterated 25 times for each of the two profiles acquired for the investigated material variants to collect a set of 50 individuals representative of the population of stress raisers present on the specimen surface. After each iteration, the elements comprised in the domain Ω were deselected to move the analysis to the next highest Von Mises stress peak, adopting a strategy already successfully applied in [45] to cast iron porosity. $\overline{W}_{rough}$ was finally used to evaluate the amplification effect exerted by surface roughness on ASED when the domain Ω is located on the specimen surface. Remembering that SED scales with the square of the stress in a linear elastic problem, the roughness-induced fatigue stress concentration K_f was evaluated as follows:

$$K_f = \sqrt{\frac{\overline{W}_{rough}}{\overline{W}_{smooth}}} \qquad (6)$$

where $\overline{W}_{smooth}$ represents the ASED in a smooth sample with same dimensions and under the same bending loading. K_f was evaluated at different fatigue lives considering the corresponding values of R_1 as plotted in Fig. 8a and treated according to the statical approach presented in the next section.

4.3. Effect of surface roughness

The simulations described in Section 4.2 permitted the generation of a population of roughness-induced stress concentration factors K_f evaluated along the 1D profiles acquired along two longitudinal line scans of total length $L = 22$ mm and positioned at the greatest distance from the neutral plane, consequently experiencing the highest bending stress.
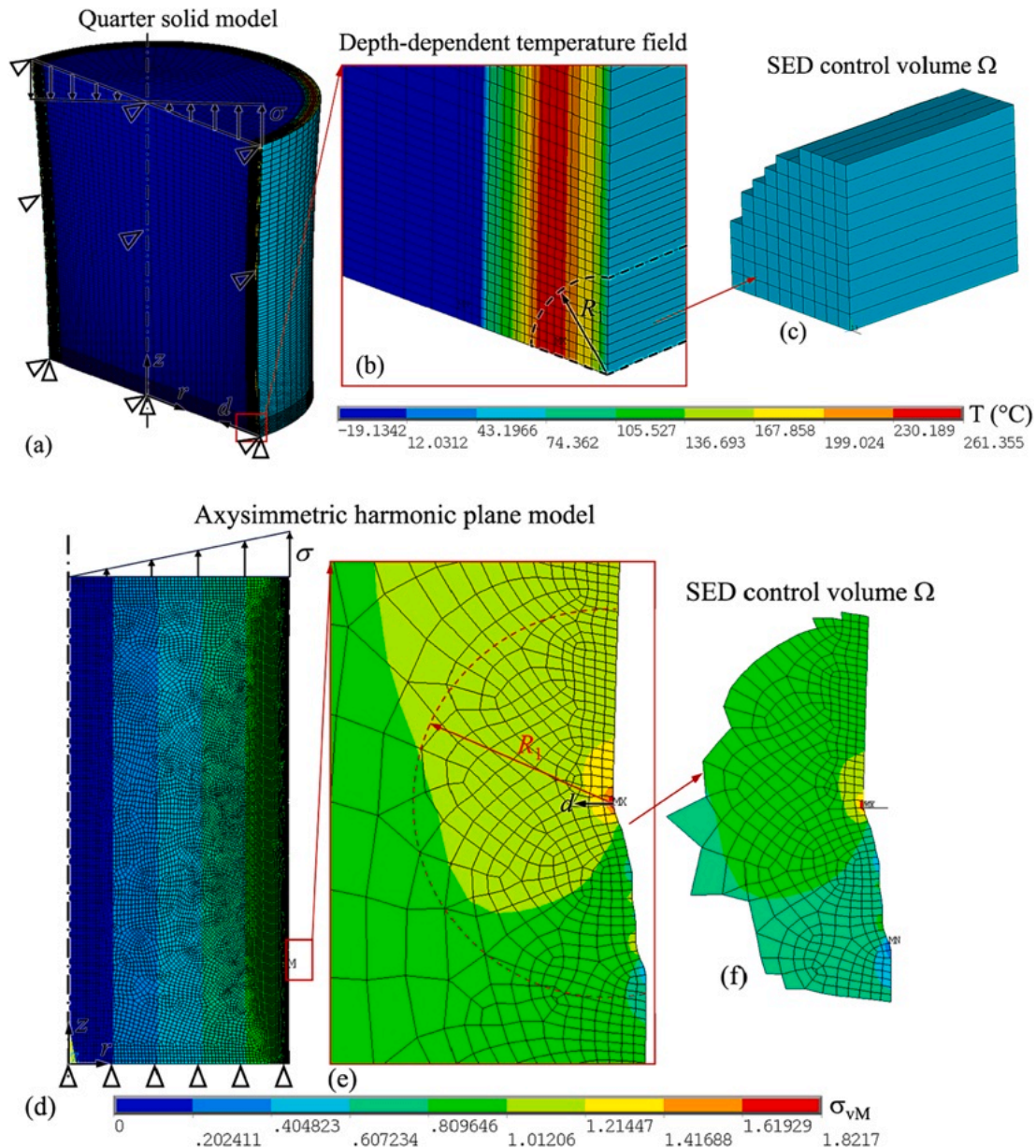
Fig. 9. (a) FE model used to assess mechanical and residual stresses in the fatigued samples. (b) Residual stresses are introduced through a fictious temperature field. (c) ASED components and specific work done by residual stresses were assessed on the control volume Ω. Harmonic axisymmetric model used to assess the stress concentration introduced by surface roughness. The measured surface profile was imported into the FE model. The ASED averaging domain Ω (f) was centered in local peaks of the equivalent von Mises stress (e).

Table 5
Parameters of Chaboche kinematic hardening submodels calibrated in [43].

C_1 (GPa)	γ_1	C_2 (GPa)	γ_2	C_3 (MPa)	γ_3	σ_0 (MPa)
126	707	2.83	1	349	0	392

C_i: Linear term of the i-th backstress component, γ_i: rate term of the i-th back-stress component, σ_0: Elastic limit after isotropic hardening saturation

These populations were statistically analyzed with the aim of estimating the expected maximum K_f according to the statistics of the largest extreme value distribution (LEVD) using the Maximum Likelihood Method [46]:

$$K_f(F) = \lambda + \delta(-\ln(-\ln(F)))$$ (7)

where F is the cumulative probability, λ and δ are the shape and the scale parameter, respectively, whose values were determined from the fit of the experimental data plotted in Fig. 10a. A similar statistical approach was successfully adopted to predict the effect of surface killer defect on the fatigue strength of additively manufactured cellular lattice materials [47]. It can be noted that the statistical distributions attest to an increment in K_f produced by all the shot peening variants with respect to the as-received conditions. Moreover, shot-peened variants employing smaller shots (UFS50 and Z100) resulted in lower K_f with respect to those adopting larger shots (Z425). The plots in Fig. 10a also permitted the estimation of $K_f^{0.99}$ corresponding to a cumulative probability F of 99 %.

A more detailed refinement of the interpretative model for surface roughness was undertaken to identify the maximum expected stress concentration factor K_f on the most stressed surface of the specimens based on the value $K_f^{0.99}$ estimated from 1D scans of the surface. Drawing inspiration from a similar approach attempted by Prof. Meneghetti and
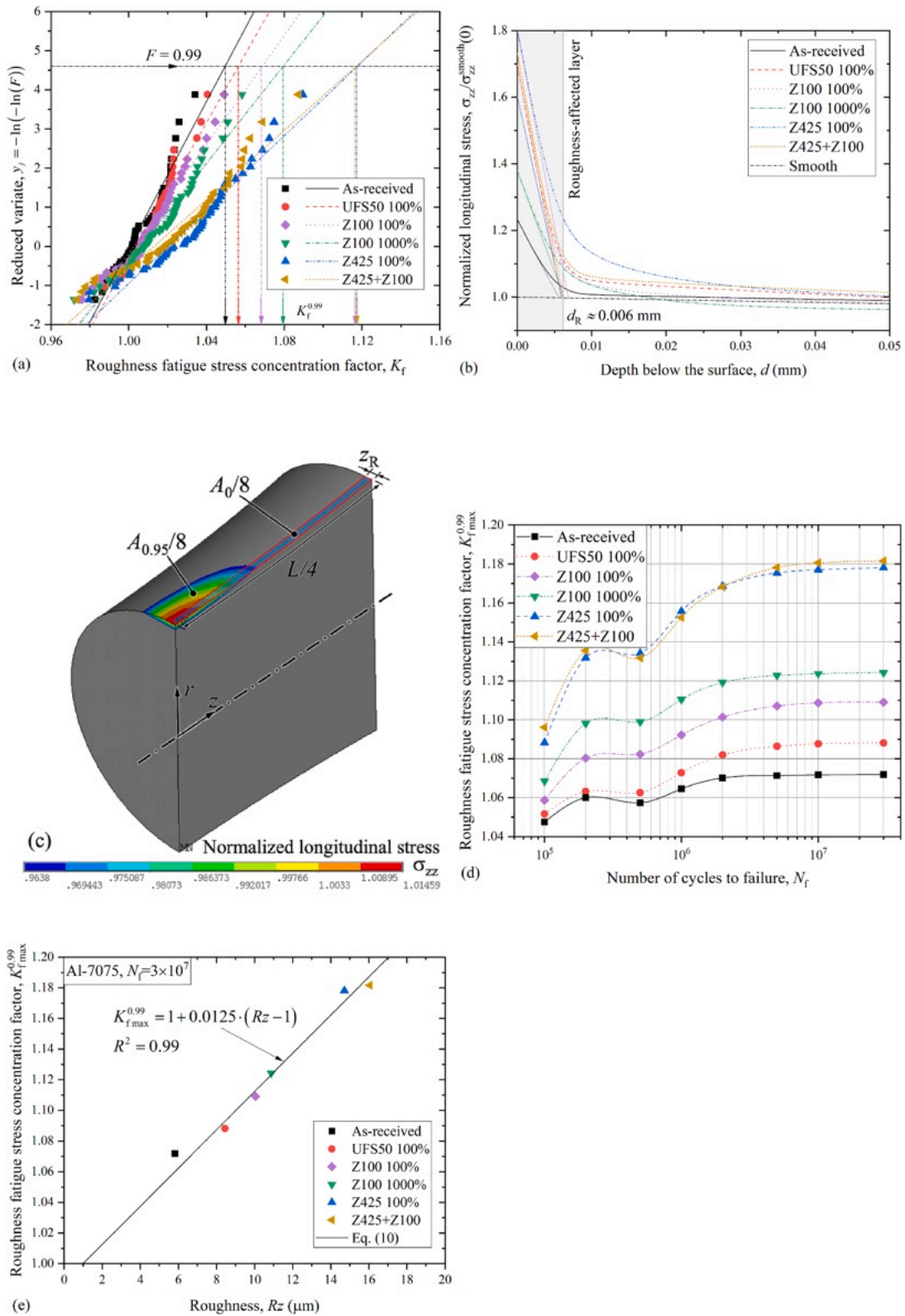
Fig. 10. (a) Cumulative probability distributions of surface roughness fatigue stress concentration factor evaluated in the investigated material variants. (b) Axial stress in-depth profile departing from a deep roughness valley under bending stress loading producing a unitary stress on the smooth surface (dash-dotted black line); thin lines represent the linearized stress distribution in the vicinity of the surface; their intersection with linearly varying bending stress was used to define the depth d_R of surface layer affected by roughness, reference frame is shown in Fig. 9e. (c) FE model of a quarter of the specimen used to assess the highly stressed surface area $A_{0.95}$ that is compared with the equivalent scanned area A_0. Note that, since the specimen is subjected to reversed bending, also the opposite surface with respect to the neutral plane must be considered, therefore the colored area represents one eight of $A_{0.95}$. (d) Variation of the maximum expected value $K_{f\,max}^{0.99}$ on $A_{0.95}$ as a function of the number of cycles to failure and its dependency upon roughness Rz.

colleagues on additively manufactured surfaces [48], the area corresponding to the line scanned during the 1D profile acquisition was estimated as follows. In Fig. 10b, the axial stress profile (extracted from the FE simulations described in Section 4.2) is plotted starting from a stress hotspot found by simulating the 1D profiles and moving radially inward from the specimen surface. Notably, the stress concentration rapidly diminishes, and the stress profile converges to that of an ideally smooth specimen under bending. The depth of material whose stress state is affected by surface roughness can be estimated by linearizing the stress profile on the surface and identifying the intersection of the linearized stress profile with the theoretical one expected in a smooth sample. The location of this intersection point is consistently found, for all material variants, at a depth denoted as d_R, approximately equal to 0.006 mm. This depth can be considered as the size of the roughness influence zone, extending along transversal directions across the stress peak. Consequently, as depicted in the schematic quarter of the specimen shown in Fig. 10c, the size of the scanned area (A_0) was evaluated as follows:

$$A_0 = 2d_R \bullet L \qquad (8)$$

Undoubtedly, the extent of A_0 may diverge from the surface area undergoing fatigue damage. A widely accepted definition for this is the region encountering more than a certain percentage of the peak stress within the specimen [49]. In this paper, we will assume that this highly stressed surface area corresponds to a percentage of 95 % of the maximum bending stress acting on the smooth gage section and therefore will be denoted as $A_{0.95}$ in Fig. 10c. It was determined through the FE model of the specimen under bending, amounting to 4.32 mm^2. The area size effect on the maximum expected K_f was estimated according to the approach proposed by Makkonen et al. [50] who introduced the following scaling factor χ_0

$$K_f(F, A_{0.95}) = [\lambda + \delta(-\ln(-\ln(F)))] \bullet \chi_0 \qquad (9a)$$

$$\chi_0 = \frac{K_f(F)}{K_f\left(F^{\frac{A_{0.95}}{A_0}}\right)}; \quad \frac{A_{0.95}}{A_0} \geq 1 \qquad (9b)$$

In the following, the maximum expected K_f will be evaluated considering a cumulative probability $F = 0.99$, which proved in [51,52] to be well correlated to the mean fatigue strength of flawed materials:

$$K_{f\,max}^{0.99} = K_f(0.99, A_{0.95}) \qquad (9c)$$

Fig. 10d plots the variation of $K_{f\,max}^{0.99}$ as a function of N_f (through the dependency of the size R_1 of the averaging domain Ω upon N_f) for the investigated materials variants. A general increasing trend of $K_{f\,max}^{0.99}$ is observed as a function of the increasing notch sensitivity at longer fatigue lives. At a fatigue life $N_f = 3 \times 10^7$ cycles, $K_{f\,max}^{0.99}$ ranges between 1.07, for the as-received condition, and 1.18, for the variants Z425 100 % and Z425 + Z100 adopting the largest shot. This latter value is in very good agreement with that estimated in [53] for the same peening treatment using a semiempirical approach based on roughness parameters. Significantly, among the various roughness parameters investigated in this study, $K_{f\,max}^{0.99}$ exhibited a notably stronger correlation with Rz. The associated trend is visualized in Fig. 10e, revealing an approximate linear relationship. This trend was utilized to fit the data, yielding the following expression:

$$K_{f\,max}^{0.99} = 1 + m(Rz - Rz_0) \qquad (10)$$

where m was determined from best-fitting and Rz_0 was set to 1 μm. This choice aligns with the widely accepted notion that Rz values lower than 1 μm have no detrimental impact on the fatigue strength [54].

5. Fatigue calculations and final discussion

The assessment of surface roughness on fatigue, as conducted in the previous section, allowed for the adjustment of the ASED components in Eq. (5), introducing $K_{f\,max}^{0.99}$ as an ASED amplification factor:

$$\Delta\overline{W} = \left(K_{f\,max}^{0.99}\right)^2 \bullet \Delta\overline{W}_{smooth} \qquad (11a)$$

$$\overline{W}_{max} = \left(K_{f\,max}^{0.99}\right)^2 \bullet \overline{W}_{max,smooth} \qquad (11b)$$

Solving Eq. (5) to determine the unknown stress amplitude (σ_a) corresponding to the fatigue strength at a given fatigue life (N_f) is not straightforward, given that the terms $\overline{W}^{RS}$, which incorporates stabilized residual stresses, depends in turn on σ_a. For this reason, an iterative solution process was adopted, the *modus operandi* of which is illustrated by the flow chart reported in Fig. 11.

In brief, for a given fatigue life N_f, $\Delta\overline{W}$ and $\overline{W}_{max}$ were calculated through finite element (FE) simulations. After initializing the iteration index i and defining the first guess value of the unknown stress amplitude σ_a^0, the initial residual stress field was introduced by means of thermal misfit strains into the FE model to calculate the specific work. Then, the equivalent ASED component was evaluated according to Eq. (5) and used to obtain the next estimate of the stress amplitude σ_a^{i+1} by assuming a quadratic relation in a small neighborhood of σ_a^i. This procedure was iterated until convergence. The procedure illustrated in Fig. 11 was performed by placing the average domain both on the specimen surface (Fig. 1b) and below the surface at a depth d_0 (Fig. 1c). In the case of the as-received condition, $\overline{W}^{RS}$ was set to zero, as negligible residual stresses were typically found in unpeened Al specimens [53]. Consequently, only the superficial crack initiation scenario depicted in Fig. 1b was simulated.

The HCF assessments of the investigated variants at $N_f = 3 \times 10^7$ are compared in Table 6 with the corresponding experimental data. The proposed ASED approach demonstrates excellent predictive accuracy for the fatigue strength of the as-received variant, affirming the suitability of the criterion calibrated on a different set of experimental specimens and its capacity to incorporate the detrimental effect of surface roughness on fatigue strength. The fatigue strength of the peened variants is accurately predicted, with a maximum absolute error of 12.6 % and 8.6 % for the calculation model assuming superficial and sub-superficial crack initiation, respectively. Overall, predictions are more accurate in the latter case, with the RMS error only at 4.7 %, compared to 8.0 % for the former case (8.7 % if only the peened variants are considered). This improved agreement with the experimental fatigue strength values aligns with fractographic inspections revealing sub-superficial crack nucleation in the peened variants.

Fig. 12a-f compares experimental SN data with fatigue predictions at different fatigue lives for all explored material variants. The following observations can be made:

The as-received variant (Fig. 12a) is accurately predicted across the entire fatigue life interval, thereby affirming the validity of the approach outlined in Section 4.3, which incorporates the influence of surface roughness into the fatigue calculation.
Superficial and sub-superficial fatigue prediction models lead to very close fatigue predictions in the case of peened variants characterized by shallow effective treatment depths d_0 (UFS50 100 %, Fig. 12b; Z100 100 %, Fig. 12c; Z100 1000 %, Fig. 12d). The predictions tend to capture the lower bound of the experimental data, delivering conservative yet accurate predictions. This is particularly evident for UFS50 100 %, where the predictions align well with high-cycle fatigue experiments terminated with failure at the lowest explored stress amplitudes. The ASED predictions consider only the impact of surface roughness and residual stresses, excluding grain refinement
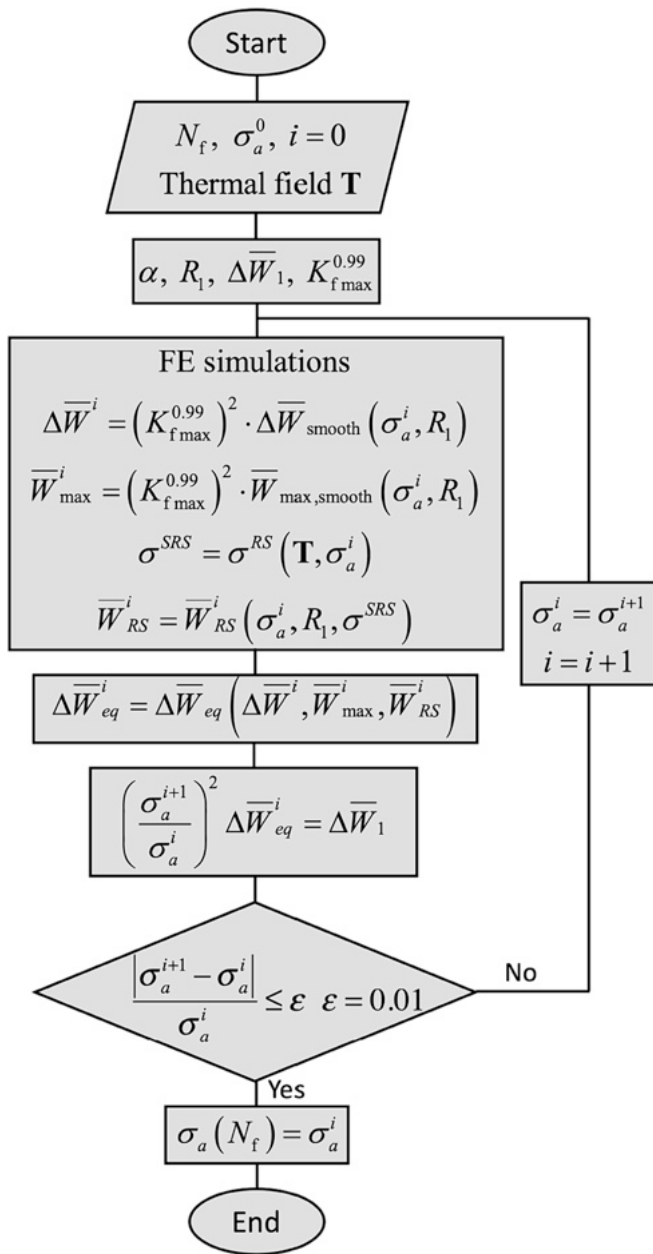
Fig. 11. Flow chart illustrating the application of the ASED fatigue criterion incorporating stabilized residual stresses.

and work hardening effects. Nevertheless, the method accurately predicts the fatigue strength of UFS50 100 % and Z100 100 %, suggesting that shot peening enhancement is more closely associated

with the effects included in the ASED model. A careful reader may object that the peened variant with the most underestimated fatigue strength (also indicated in Table 6) is UFS50 100 %, where the contribution of work hardening (as evident in microhardness profiles, Fig. 4b) to fatigue enhancement is the highest among the investigated conditions. However, this contribution can be estimated to be less than 10 %, viz. the order of magnitude of the prediction error in fatigue strength.

In the variants displaying deeper treatment depths d_0 (Z425 100 %, Fig. 12e; Z425 + Z100, Fig. 12f), the discrepancy between the two predictive models is more pronounced. Additionally, predictions assuming sub-superficial crack initiation show significantly better agreement with the trend exhibited by the experimental data. Notably, when focusing on the Z425 variant, the sub-superficial fatigue calculation model better predicts experiments denoted as S11 (Fig. 6f) and S13 (Fig. 6g), where crack initiation occurred at a depth comparable to the treatment depth, d_0. Conversely, the experiment denoted as S4 (Fig. 6e), resulting in crack initiation closer to the outer surface, is better predicted by the model assuming surface crack initiation.

A conservative predictive approach suggests performing both simulation approaches and considering the predictions of the model with the lowest estimates. In this case, the predictions capture very well the lower bound of the experimental data.

Fig. 13a and b show the relationship between predicted stress amplitude and experimental stress amplitude for all investigated conditions, considering near-surface and sub-superficial crack initiation, respectively. The latter approach has proven to provide the most accurate predictions (lower total RMS error), marked by a higher level of conservatism, as indicated by more predictions lying on the right side with respect to the bisector.

The very good accuracy demonstrated by the devised fatigue calculation model, even though it does not explicitly consider work-hardening and grain refinement effects, suggests that these mechanisms may play a negligible role in determining fatigue strength. Provided that a shot peening treatment is correctly designed to inhibit the detrimental effect of surface roughness and pile-up defects, it appears that its predominant beneficial effect is closely associated with the introduction of compressive residual stresses. To this regard, it can be argued that shot peening treatments leading to an in-depth residual compressive stress profile with a peak near the surface and rapidly decreasing inward into the specimen are more effective in improving the fatigue strength of Al alloys, especially when tested under bending loading. This is in contrast to more intense surface treatments that position the peak deeper below the surface and exhibit a slower decay in-depth residual stress profile. This interpretative key is outlined in Fig. 14, where treatments denoted as "I" and "II" correspond to the former and latter types, respectively. When computing the specific work done by residual stresses, the averaging domain Ω will sample much more intense compressive residual stress in case I compared to case II, resulting in a more pronounced fatigue enhancement. Overpeening

Table 6
High-cycle ($N_f = 3 \times 10^7$) fatigue strength assessments of the investigated conditions.

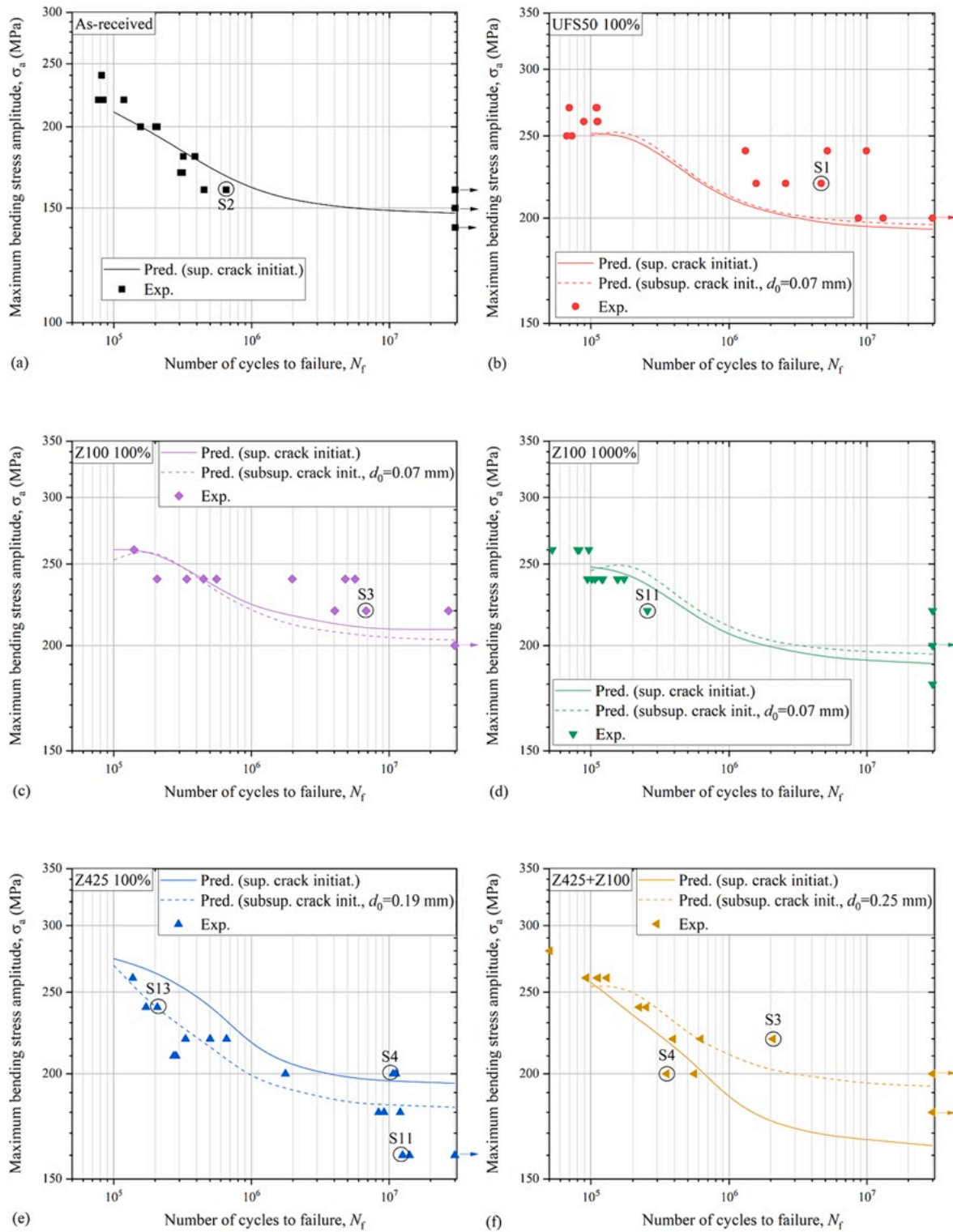| Condition	Exp. $\sigma_{a,3\times10^7}$ (MPa)	Standard deviation, S (MPa)	Pred. $\sigma_{a,3\times10^7}$ (MPa)		Error (%)	
			Sup. (Fig. 1b)	Sub-sup. (Fig. 1c)	Sup. (Fig. 1b)	Sub-sup. (Fig. 1c)
As-received	147	10	147	–	0.2	–
UFS50 100 %	215	15	194	196	−9.8	−8.6
Z100 100 %	211	15	209	203	−1.0	−3.7
Z100 1000 %	200	9.9	190	196	−4.8	−2.3
Z425 100 %	177	14	195	182	10.1	3.1
Z425 + Z100	188	12	164	193	−12.6	2.8
Max absolute error (%)					12.6	8.6
RMS error (%)					8.0 (8.7*)	4.7
*Excluding the as-received variant						

Fig. 12. Assessment of the fatigue curves of the investigated conditions, assuming either near-superficial (solid line) or sub-superficial crack initiation (dashed line). The dots indicate the experimental data. (a) As-received condition, (b) UFS50 100 %, (c) Z100 100 %, (d) Z100 1000 %, (e) Z425 100 %, (f) Z425 100 % + Z100 1000 % shot peened conditions.

treatments at high coverage (like Z100 1000 %) do not substantially modify this scenario and therefore do not lead to further fatigue improvement compared to case I. On the contrary, overpeening can be counterproductive, as it might attenuate the near-surface compressive residual stress peak.

6. Conclusions

In this study, the effects of shot peening treatments on the fatigue behavior of Al alloy specimens were systematically investigated. The experimental results, along with comprehensive fractographic inspections and fatigue calculation models, provide valuable insights into
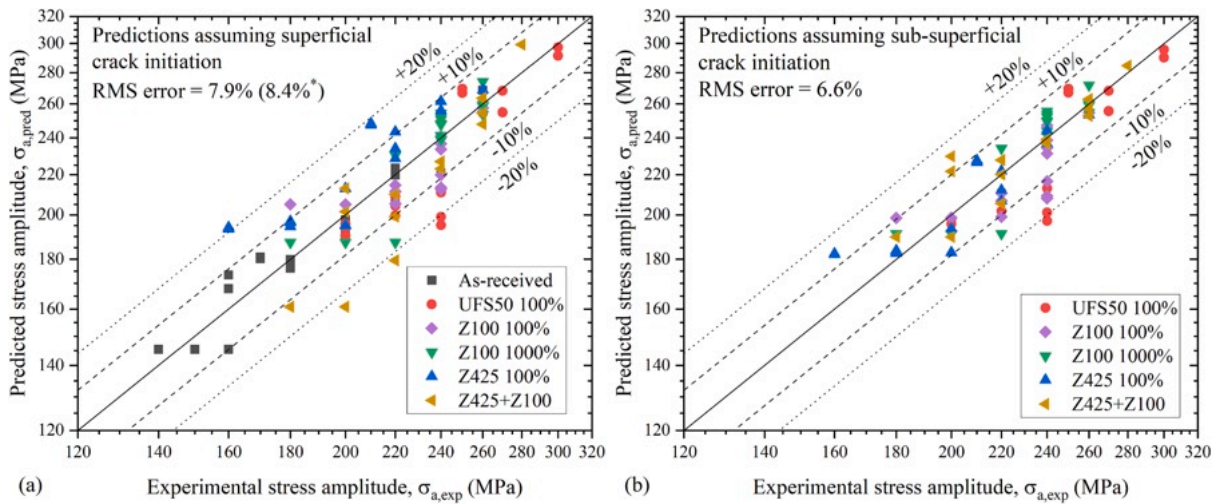
Fig. 13. Fatigue predictions in terms of predicted stress amplitude versus experimental stress amplitude for all the investigated conditions. The fatigue calculations were made considering (a) surface and (b) sub-superficial crack initiation. *Excluding the as-received variant.
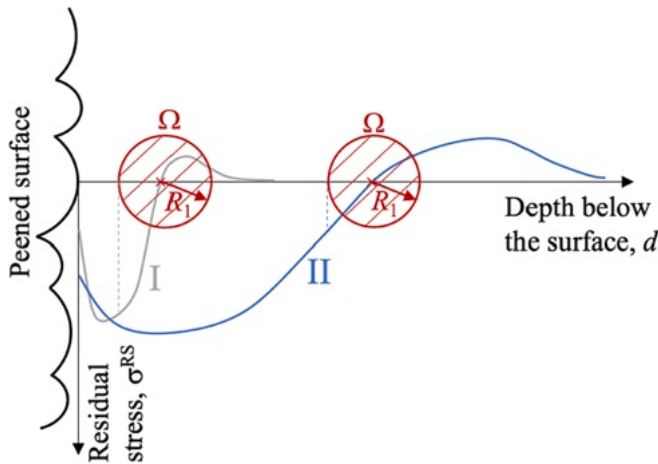

Fig. 14. Illustration depicting shot peening treatments and their resulting residual stress profiles: (I) featuring an in-depth pattern of compressive stresses with a peak near the surface and a rapid decrease inward into the specimen, or (II) showcasing a profile with the peak situated deeper below the surface and slowly diminishing toward the specimen's interior. Dashed lines denote the residual stress magnitude at the boundary of the ASED averaging domain (Ω) when positioned below the surface at the treatment's effective depth (d_0).

the impact of shot peening parameters on fatigue performance.

The findings can be summarized as follows:

1. Surface Roughness and Microhardness:
   o Peening treatments induced an increase in surface roughness, with a discernible trend based on shot size.
   o Microhardness profiles showed variations, with UFS50 treatment exhibiting slightly higher microhardness in the surface layer.
2. Residual Stress and Strain Profiles:
   o In-depth measurements illustrated the dependence of residual stresses and strains on shot size, with larger shots leading to higher values.
   o Peening depth (d_0) varied among treatments, with Z100 100 % and Z425 100 % exhibiting the deepest compressive residual stress peaks.
3. Fatigue Life Improvement:
   o All peening treatments effectively prolonged the fatigue life of the material.

   o The degree of improvement depended on applied load levels, with gentle treatments (UFS50 100 % and Z100 100 %) showing the highest enhancements.
4. Fatigue Crack Initiation:
   o Fractographic analysis revealed dualism in fatigue crack initiation locations, with shallow initiation in treatments employing smaller shots and deeper initiation in treatments with larger shots.
5. Fatigue Calculation Model:
   o The Average Strain-Energy-Density (ASED) criterion, incorporating the effects of residual stresses and surface roughness, was employed for fatigue predictions.
   o The model accurately predicted fatigue strength for the as-received variant and demonstrated good accuracy for peened variants, especially if sub-superficial crack initiation in peened variants was considered.
   o Fatigue improvement due to shot peening is satisfactorily modelled including only surface roughness and residual stresses. Grain refinement and work hardening seem to play a marginal role.
6. Surface Roughness Influence:
   o The fatigue stress concentration factor $K_{f\,max}^{0.99}$ proved to capture the detrimental effect of surface roughness on the fatigue strength.
   o A linear relationship between $K_{f\,max}^{0.99}$ and Rz was found, suggesting a simple evaluation tool of the effect of surface roughness on the fatigue strength of shot peened Al alloys.
7. Optimal Peening Depth for Fatigue Enhancement:
   o Treatments resulting in an in-depth residual compressive stress profile near the surface were more effective in improving fatigue strength with respect to more intense treatments producing a deeper compressive residual stress peak accompanied by a slow residual stress extinction inward the specimen interior.
   o Overpeening at high coverage showed attenuation of near-surface compressive residual stress and does not result in further fatigue strength enhancement.

CRediT authorship contribution statement

M. Benedetti: Writing – review & editing, Writing – original draft, Validation, Investigation, Funding acquisition, Formal analysis, Data curation, Conceptualization. **M. Pedranz:** Writing – review & editing, Investigation, Data curation. **V. Fontanari:** Writing – review & editing, Conceptualization. **C. Menapace:** Writing – review & editing, Investigation. **M. Bandini:** Writing – review & editing, Resources.

Declaration of competing interest

The authors declare that they have no known competing financial interests or personal relationships that could have appeared to influence the work reported in this paper.

Data availability

Data will be made available on request.

Appendix A

A.1. Fatigue data of as-received (unpeened) condition.

As-received condition.

Sample ID	Stress amplitude, σ_a (MPa)	Number of cycles to failure, N_f	Notes
1	180	320,113	
2	160	654,210	
3	140	30,000,000	Run-out
3	200	206,546	Retest
4	150	30,000,000	
5	220	118,411	
6	160	452,945	
7	150	30,000,000	Run-out
8	160	30,000,000	Run-out
9	180	388,940	
10	200	156,471	
11	200	201,365	
12	220	84,034	
13	220	77,142	
7	240	81,704	Retest
8	260	33,915	Retest
14	170	304,997	

A.2. Fatigue data of UFS50 100 % condition.

UFS50 100% condition.

Sample ID	Stress amplitude, σ_a (MPa)	Number of cycles to failure, N_f	Notes
1	220	4,659,906	
2	220	2,572,887	
3	200	8,673,798	
4	220	1,569,785	
5	200	30,000,000	Run-out
5	300	31,530	Retest
6	200	13,117,910	
7	240	1,313,252	
8	240	9,930,751	
9	240	5,160,408	
10	300	36,354	
11	270	69,871	
12	270	109,562	
13	260	111,363	
14	260	89,002	
15	250	67,069	

A.3. Fatigue data of Z100 100 % condition.

Z100 100% condition.

Sample ID	Stress amplitude, σ_a (MPa)	Number of cycles to failure, N_f	Notes
1	160	30,000,000	Run-out
1	240	4,809,077	Retest
2	240	339,579	
3	220	6,811,427	
4	200	30,000,000	
5	240	206,588	
6	180	30,000,000	
7	240	5,667,766	
8	200	30,000,000	
9	240	559,569	
10	260	140,597	

(continued on next page)

(*continued*)

Sample ID	Stress amplitude, σ_a (MPa)	Number of cycles to failure, N_f	Notes
11	240	1,982,830	
12	240	449,172	
13	220	4,031,536	

A.4. Fatigue data of Z100 1000 % condition.

Z100 1000% condition.

Sample ID	Stress amplitude, σ_a (MPa)	Number of cycles to failure, N_f	Notes
1	200	30,000,000	
2	240	120,804	
3	220	30,000,000	
4	240	101,791	
5	240	154,247	
6	180	30,000,000	Run-out
7	240	107,473	
6	260	80,234	Retest
8	260	52,486	
9	260	82,481	
10	160	30,000,000	Run-out
10	240	94,659	Retest
11	220	254,793	
12	240	155,526	
13	200	30,000,000	
14	240	172,603	
15	240	118,705	

A.5. Fatigue data of Z425 100 % condition.

Z425 100% condition.

Sample ID	Stress amplitude, σ_a (MPa)	Number of cycles to failure, N_f	Notes
1	220	332,194	
2	220	501,417	
3	200	11,204,332	
4	200	10,688,585	
5	200	1,767,104	
6	220	661,207	
7	180	8,393,797	
8	180	12,035,696	
9	180	9,198,086	
10	160	12,528,471	
11	160	14,068,460	
12	160	30,000,000	Run-out
12	240	207,663	Retest
13	240	171,869	
14	260	137,639	
15	210	273,163	
16	210	283,656	

A.6. Fatigue data of Z425 + Z100 condition.

Z425 + Z100 condition.

Sample ID	Stress amplitude, σ_a (MPa)	Number of cycles to failure, N_f	Notes
1	260	93,197	
2	240	222,272	
3	220	2,079,267	
4	200	351,605	
5	180	30,000,000	Run-out
5	260	129,328	Retest
6	260	111,671	
7	240	250,100	
8	220	621,705	
9	200	30,000,000	Run-out
9	280	50,526	Retest
10	220	392,358	
11	200	558,751	
12	180	30,000,000	Run-out
12	260	92,485	Retest

Appendix B

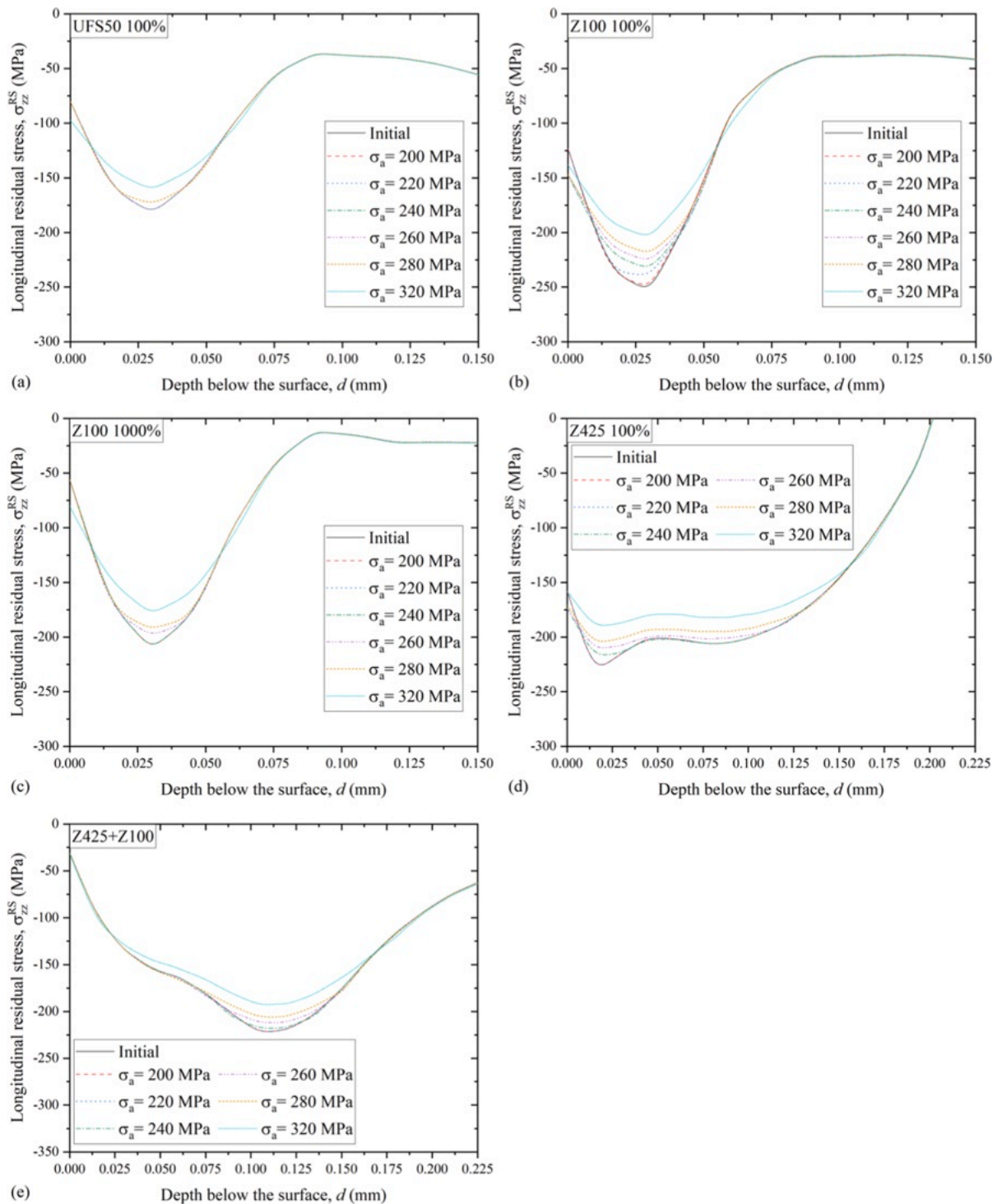*Numerically evaluated initial and residual stress profiles.*

Fig. B1. Initial and stabilized residual stress in-depth profiles evaluated according to the numerical procedure described in Section 4.2. σa denotes the stress amplitude of the fully reversed bending fatigue load. The stabilized profiles are evaluated after the application of 20 fatigue cycles. (a) UFS50 100 %, (b) Z100 100 %, (c) Z100 1000 %, (d) Z425 100 %, (e) Z425 100 % + Z100 1000 % shot peened conditions.

References

[1] Handbook ASM. Properties and Selection: Nonferrous Alloys and Special-Purpose Materials, Vol. 2. ASM International; 1990.

[2] Zhao T, Jiang Y. Fatigue of 7075–T651 aluminum alloy. Int J Fatigue 2008;30: 834–49. https://doi.org/10.1016/j.ijfatigue.2007.07.005.

[3] Dursun T, Soutis C. Recent developments in advanced aircraft aluminium alloys. Mater Des 2014;56:862–71. https://doi.org/10.1016/j.matdes.2013.12.002.

[4] Melhem GN. Aerospace Fasteners: Use in Structural Applications. In: Encycl. Alum. Its Alloy. Boca Raton; CRC Press: 2019. Doi: 10.1201/9781351045636-140000240.

[5] Nasab MH, Gastaldi D, Lecis NF, Vedani M. On morphological surface features of the parts printed by selective laser melting (SLM). Addit Manuf 2018;24:373–7. https://doi.org/10.1016/j.addma.2018.10.011.

[6] Ferro P, Fabrizi A, Berto F, Savio G, Meneghello R, Rosso S. Defects as a root cause of fatigue weakening of additively manufactured AlSi10Mg components. Theor Appl Fract Mech 2020;108:102611. https://doi.org/10.1016/j.tafmec.2020.102611.

[7] Bagherifard S. Enhancing the structural performance of lightweight metals by shot peening. Adv Eng Mater 2019;21:1801140. https://doi.org/10.1002/adem.201801140.

[8] Maleki E, Bagherifard S, Unal O, Shao S, Shamsaei N, Guagliano M. Assessing the efficacy of several impact-based mechanical techniques on fatigue behavior of additive manufactured AlSi10Mg. Mater Sci Eng A 2023;872:144940. https://doi.org/10.1016/j.msea.2023.144940.

[9] Luong H, Hill MR. The effects of laser peening and shot peening on high cycle fatigue in 7050–T7451 aluminum alloy. Mater Sci Eng A 2010;527:699–707. https://doi.org/10.1016/j.msea.2009.08.045.

[10] R, p,. The influence of compressive residual stress on metallurgical and mechanical properties of materials exposed to shot peening: a review. Can Metall Q 2023:1–41. https://doi.org/10.1080/00084433.2023.2213045.

[11] Wagner L. Mechanical surface treatments on titanium, aluminum and magnesium alloys. Mater Sci Eng A 1999;263:210–6. https://doi.org/10.1016/S0921-5093(98)01168-X.

[12] Gariépy A, Bridier F, Hoseini M, Bocher P, Perron C, Lévesque M. Experimental and numerical investigation of material heterogeneity in shot peened aluminium alloy AA2024-T351. Surf Coatings Technol 2013;219:15–30. https://doi.org/10.1016/j.surfcoat.2012.12.046.

[13] Gao Y, Lu F, Yao M. Influence of mechanical surface treatments on fatigue property of 30CrMnSiNi2A steel. Surf Eng 2005;21:325–8. https://doi.org/10.1179/174329405X40957.

[14] Miller KJ. THE two thresholds of fatigue behaviour. Fatigue Fract Eng Mater Struct 1993;16:931–9. https://doi.org/10.1111/j.1460-2695.1993.tb00129.x.

[15] Delosrios E, Walley A, Milan M, Hammersley G. Fatigue crack initiation and propagation on shot-peened surfaces in A316 stainless steel. Int J Fatigue 1995;17:493–9. https://doi.org/10.1016/0142-1123(95)00044-T.

[16] Rodopoulos C. Optimisation of the fatigue resistance of 2024–T351 aluminium alloys by controlled shot peening—methodology, results and analysis. Int J Fatigue 2004;26:849–56. https://doi.org/10.1016/j.ijfatigue.2004.01.003.

[17] Hammond DW, Meguid SA. Crack propagation in the presence of shot-peening residual stresses. Eng Fract Mech 1990;37:373–87. https://doi.org/10.1016/0013-7944(90)90048-L.

[18] Benedetti M, Fontanari V, Bandini M, Savio E. High- and very high-cycle plain fatigue resistance of shot peened high-strength aluminum alloys: the role of surface morphology. Int J Fatigue 2015;70:451–62. https://doi.org/10.1016/j.ijfatigue.2014.07.002.

[19] Oguri K. Fatigue life enhancement of aluminum alloy for aircraft by fine particle shot peening (FPSP). J Mater Process Technol 2011;211:1395–9. https://doi.org/10.1016/j.jmatprotec.2011.03.011.

[20] Ferreira N, Jesus JS, Ferreira JAM, Capela C, Costa JM, Batista AC. Effect of bead characteristics on the fatigue life of shot peened Al 7475–T7351 specimens. Int J Fatigue 2020;134:105521. https://doi.org/10.1016/j.ijfatigue.2020.105521.

[21] Gao YK. Improvement of fatigue property in 7050–T7451 aluminum alloy by laser peening and shot peening. Mater Sci Eng A 2011;528:3823–8. https://doi.org/10.1016/j.msea.2011.01.077.

[22] Benedetti M. Bending fatigue behaviour of differently shot peened Al 6082 T5 alloy. Int J Fatigue 2004;26:889–97. https://doi.org/10.1016/j.ijfatigue.2003.12.003.

[23] Hassani-Gangaraj SM, Cho KS, Voigt H-J-L, Guagliano M, Schuh CA. Experimental assessment and simulation of surface nanocrystallization by severe shot peening. Acta Mater 2015;97:105–15. https://doi.org/10.1016/j.actamat.2015.06.054.

[24] Trško L, Guagliano M, Bokůvka O, Nový F, Jambor M, Florková Z. Influence of severe shot peening on the surface state and ultra-high-cycle fatigue behavior of an AW 7075 aluminum alloy. J Mater Eng Perform 2017;26:2784–97. https://doi.org/10.1007/s11665-017-2692-9.

[25] Benedetti M, Fontanari V, Allahkarami M, Hanan JC, Bandini M. On the combination of the critical distance theory with a multiaxial fatigue criterion for predicting the fatigue strength of notched and plain shot-peened parts. Int J Fatigue 2016;93:133–47. https://doi.org/10.1016/j.ijfatigue.2016.08.015.

[26] Gerin B, Pessard E, Morel F, Verdu C. A non-local approach to model the combined effects of forging defects and shot-peening on the fatigue strength of a pearlitic steel. Theor Appl Fract Mech 2018;93:19–32. https://doi.org/10.1016/j.tafmec.2017.06.012.

[27] Hemmesi K, Farajian M, Fatemi A. Application of the critical plane approach to the torsional fatigue assessment of welds considering the effect of residual stresses. Int J Fatigue 2017;101:271–81. https://doi.org/10.1016/j.ijfatigue.2017.01.023.

[28] Santus C, Romanelli L, Grossi T, Bertini L, Le Bone L, Chiesi F, et al. Elastic–plastic analysis of high load ratio fatigue tests on a shot-peened quenched and tempered steel, combining the Chaboche model and the theory of critical distances. Int J Fatigue 2023;174:107713. https://doi.org/10.1016/j.ijfatigue.2023.107713.

[29] Servetti G, Zhang X. Predicting fatigue crack growth rate in a welded butt joint: the role of effective R ratio in accounting for residual stress effect. Eng Fract Mech 2009;76:1589–602. https://doi.org/10.1016/j.engfracmech.2009.02.015.

[30] Vázquez J, Navarro C, Domínguez J. A model to predict fretting fatigue life including residual stresses. Theor Appl Fract Mech 2014;73:144–51. https://doi.org/10.1016/j.tafmec.2014.06.012.

[31] Benedetti M, Berto F, Marini M, Raghavendra S, Fontanari V. Incorporating residual stresses into a strain-energy-density based fatigue criterion and its application to the assessment of the medium-to-very-high-cycle fatigue strength of shot-peened parts. Int J Fatigue 2020;139:105728. https://doi.org/10.1016/j.ijfatigue.2020.105728.

[32] Curtis S, Delosrios E, Rodopoulos C, Levers A. Analysis of the effects of controlled shot peening on fatigue damage of high strength aluminium alloys. Int J Fatigue 2003;25:59–66. https://doi.org/10.1016/S0142-1123(02)00049-X.

[33] Fathallah R. High cycle fatigue behavior prediction of shot-peened parts. Int J Fatigue 2004;26:1053–67. https://doi.org/10.1016/j.ijfatigue.2004.03.007.

[34] Fernández-Pariente I, Bagherifard S, Guagliano M, Ghelichi R. Fatigue behavior of nitrided and shot peened steel with artificial small surface defects. Eng Fract Mech 2013;103:2–9. https://doi.org/10.1016/j.engfracmech.2012.09.014.

[35] Shiozawa K, Lu L. Very high-cycle fatigue behaviour of shot-peened high-carbon–chromium bearing steel. Fatigue Fract Eng Mater Struct 2002;25:813–22. https://doi.org/10.1046/j.1460-2695.2002.00567.x.

[36] Pyttel B, Brunner I, Kaiser B, Berger C, Mahendran M. Fatigue behaviour of helical compression springs at a very high number of cycles – investigation of various influences. Int J Fatigue 2014;60:101–9. https://doi.org/10.1016/j.ijfatigue.2013.01.003.

[37] Benedetti M, Menapace C, Fontanari V, Santus C. On the variability in static and cyclic mechanical properties of extruded 7075–T6 aluminum alloy. Fatigue Fract Eng Mater Struct 2021;44:2975–89. https://doi.org/10.1111/ffe.13530.

[38] Moore MG, Evans WP. Mathematical correction for stress in removed layers in X-ray diffraction residual stress analysis. SAE Trans 1958;66:340–5.

[39] Benedetti M, Berto F, Le Bone L, Santus C. A novel strain-energy-density based fatigue criterion accounting for mean stress and plasticity effects on the medium-to-high-cycle uniaxial fatigue strength of plain and notched components. Int J Fatigue 2020;133:105397. https://doi.org/10.1016/j.ijfatigue.2019.105397.

[40] Santus C, Taylor D, Benedetti M. Experimental determination and sensitivity analysis of the fatigue critical distance obtained with rounded V-notched specimens. Int J Fatigue 2018;113:113–25. https://doi.org/10.1016/j.ijfatigue.2018.03.037.

[41] Benedetti M, Fontanari V, Winiarski B, Allahkarami M, Hanan JCC. Residual stresses reconstruction in shot peened specimens containing sharp and blunt notches by experimental measurements and finite element analysis. Int J Fatigue 2016;87:102–11. https://doi.org/10.1016/j.ijfatigue.2016.01.020.

[42] Benedetti M, Fontanari V, Monelli BD. Numerical simulation of residual stress relaxation in shot peened high-strength aluminum alloys under reverse bending fatigue. J Eng Mater Technol 2010;132. https://doi.org/10.1115/1.3184083.

[43] Santus C, Grossi T, Romanelli L, Pedranz M, Benedetti M. A computationally fast and accurate procedure for the identification of the Chaboche isotropic-kinematic hardening model parameters based on strain-controlled cycles and asymptotic ratcheting rate. Int J Plast 2023;160:103503. https://doi.org/10.1016/j.ijplas.2022.103503.

[44] Benedetti M, Santus C, Berto F. Inverse determination of the fatigue strain energy density control radius for conventionally and additively manufactured rounded V-notches. Int J Fatigue 2019;126:306–18. https://doi.org/10.1016/j.ijfatigue.2019.04.040.

[45] Pedranz M, Fontanari V, Raghavendra S, Santus C, Zanini F, Carmignato S, et al. A new energy based highly stressed volume concept to investigate the notch-pores interaction in thick-walled ductile cast iron subjected to uniaxial fatigue. Int J Fatigue 2023;169:107491. https://doi.org/10.1016/j.ijfatigue.2022.107491.

[46] Beretta S, Murakami Y. Statistical analysis of defects for fatigue strength prediction and quality control of materials. Fatigue Fract Eng Mater Struct 1998;21:1049–65. https://doi.org/10.1046/j.1460-2695.1998.00104.x.

[47] Raghavendra S, Dallago M, Zanini F, Carmignato S, Berto F, Benedetti M. A probabilistic average strain energy density approach to assess the fatigue strength of additively manufactured cellular lattice materials. Int J Fatigue 2023;172:107601. https://doi.org/10.1016/j.ijfatigue.2023.107601.

[48] Rigon D, Coppola F, Meneghetti G. Fracture mechanics-based analysis of the fatigue limit of Ti6Al4V alloy specimens manufactured by SLM in as-built surface conditions by means of areal measurements. Eng Fract Mech 2024;295:109720. https://doi.org/10.1016/j.engfracmech.2023.109720.

[49] Marques JME, Mžourek M, Papuga J, Růžička M, Benasciutti D. A probabilistic stress-life model supported by weakest link principle and highly-stressed volume/surface area concepts. Int J Fatigue 2024;178:108006. https://doi.org/10.1016/j.ijfatigue.2023.108006.

[50] Makkonen L, Rabb R, Tikanmäki M. Size effect in fatigue based on the extreme value distribution of defects. Mater Sci Eng A 2014;594:68–71. https://doi.org/10.1016/j.msea.2013.11.045.

[51] Emanuelli L, Molinari A, Facchini L, Sbettega E, Carmignato S, Bandini M, et al. Effect of heat treatment temperature and turning residual stresses on the plain and notch fatigue strength of Ti-6Al-4V additively manufactured via laser powder bed fusion. Int J Fatigue 2022;162:107009. https://doi.org/10.1016/j.ijfatigue.2022.107009.

[52] Benedetti M, Santus C, Raghavendra S, Lusuardi D, Zanini F, Carmignato S. Multiaxial plain and notch fatigue strength of thick-walled ductile cast iron EN-GJS-600-3: combining multiaxial fatigue criteria, theory of critical distances, and

defect sensitivity. Int J Fatigue 2022;156:106703. https://doi.org/10.1016/j.ijfatigue.2021.106703.

[53] Benedetti M, Fontanari V, Scardi P, Ricardo CLA, Bandini M. Reverse bending fatigue of shot peened 7075–T651 aluminium alloy: the role of residual stress

relaxation. Int J Fatigue 2009;31:1225–36. https://doi.org/10.1016/j.ijfatigue.2008.11.017.

[54] H. Wittel, C. Spura, D. Jannasch, Roloff/Matek Maschinenelemente, Springer Fachmedien Wiesbaden, Wiesbaden, 2021. Doi: 10.1007/978-3-658-34160-2.